ORIGINAL RESEARCH ARTICLE

Quenching and Partitioning (Q&P) Steel: Alloy Design, Phase Transformation and Evolution of Microstructure

SACHIN KUMAR and SHIV BRAT SINGH

A low-carbon low-alloy steel suitable for Q&P processing was designed by considering the influence of alloying elements on various aspects of transformation and microstructure like the optimum quenching temperature (QT^{opt}) that maximizes the amount of retained austenite at room temperature, the critical cooling rate for martensite transformation, thermal and mechanical stability of retained austenite and cementite precipitation from austenite. A number of semi-empirical equations and the thermodynamic software ThermoCalc were used for the purpose. The designed steel was prepared and pre-processed in the laboratory by melting, casting and hot forging. The samples from the as forged material were then subjected to quenching, austempering and quenching and partitioning treatments in a dilatometer and salt-bath furnace to understand the preliminary phase transformation behavior, microstructural evolution and mechanical properties. An alternative method, utilizing the experimental dilatation data obtained during quenching and conventional austempering processes, was used to quantify the multiphase Q&P microstructures which provided a reasonably accurate estimate of the actual amount of retained austenite at room temperature. The microstructure obtained after Q&P processing resulted in a better combination of strength and elongation than the martensitic and bainitic microstructures which was attributed to a more effective exploitation of the TRIP effect. The TRIP behavior has been found to depend not only on the amount of retained austenite and its carbon content but also on the morphology of austenite and the characteristics of the surrounding phases.

https://doi.org/10.1007/s11661-023-07085-x

I. INTRODUCTION

THE quenching and partitioning (Q&P) process is a relatively new processing route proposed by Speer *et al.*[1] to produce advanced high strength steel (AHSS) grades. The Q&P process involves austenitization followed by quenching to a predetermined quenching temperature (QT) between the M_s (martensite-start) and M_f (martensite-finish) temperatures where austenite partially transforms to martensite leaving some untransformed austenite. Then, a partitioning step at the QT or at a temperature below or above M_s is introduced where partitioning of carbon from supersaturated martensite to untransformed austenite occurs.[1,2] The partitioning step is followed by final quenching to room temperature (RT) during which the carbon enriched austenite can transform partially to fresh martensite or get stabilized completely in the resultant microstructure depending on its carbon enrichment.[1–3] In general, the Q&P microstructure consists of retained austenite dispersed within decarburized martensite.[4–6] The formation of other microstructural features such as carbides[7–9] and bainitic-ferrite[10–12] is also possible during the Q&P processing.

Some of the important aspects which must be considered for designing the Q&P steels are: (i) the steel must have sufficient hardenability to suppress the formation of high temperature transformation products like ferrite, pearlite *etc.* and to ensure martensite formation at lower cooling rates, (ii) retention of a higher retained austenite fraction having moderate stability, (iii) retardation of the competing reactions for example carbide formation and bainite transformation and of course, (iv) the cost.

The hardenability of steels depends on a number of factors such as its composition, prior austenite grain size, the severity of quench and size of the specimen.[13,14] Alloying elements such as C, Mn, Mo, Cr, Ni and higher prior austenite grain size improve the

SACHIN KUMAR and SHIV BRAT SINGH are with the Department of Metallurgical and Materials Engineering, Indian Institute of Technology Kharagpur, Kharagpur 721 302, India. Contact e-mail: sachin.kumarits@gmail.com
Manuscript submitted August 10, 2022; accepted May 4, 2023.
Article published online June 6, 2023

hardenability of steels.[14–16] On the other hand, Si and Al shift the time–temperature-transformation diagram of ferrite to left[17] and hence decrease the hardenability of steel.

The mechanical properties of the Q&P steels are dictated to a large extent by deformation-induced transformation of austenite to martensite,[8,18–20] which is usually known as transformation-induced plasticity (TRIP) effect.[21] A higher retained austenite fraction having moderate stability is advantageous for better exploitation of the TRIP effect.[22–24] The amount of retained austenite at *RT* depends mainly on the alloy composition as well as on the Q&P processing parameters such as the quenching temperature (*QT*), partitioning temperature (*PT*) and partitioning time (t_p).[8,25] The *QT* that maximizes the amount of retained austenite at *RT* is known as the optimum *QT* (QT^{opt}) and is one of the vital design parameters of the Q&P process.

The formation of carbides decreases the solute carbon content of austenite thereby decreasing its stability and the amount of retained austenite at *RT*.[12,26,27] Similarly, bainite transformation, if it takes place, also consumes a part of austenite.[9,26] Therefore, control over these competing reactions is necessary to enhance the effectiveness of the Q&P process. Although complete suppression of these competing reactions is very difficult, appropriate choice of alloy chemistry and process parameters is found beneficial for retarding these reactions to some extent and thereby enhancing the effectiveness of the Q&P treatment. In this work, instead of a trial and error approach, sound physical metallurgy principles were used to design a low-carbon (0.2 wt pct) low alloy steel where calculations using published semi empirical equations[28–33] and ThermoCalc software were performed to optimize the composition.

The quantification of multiphase Q&P microstructures is very difficult using standard metallographic techniques. In this work, an alternate method, which utilizes the experimental dilatation data, has been employed for the quantification of multiphase Q&P microstructure. It is noteworthy that dilatation data give the real time monitoring of the solid–solid phase transformation in steels and can be employed for the quantification of these complex microstructures.[12,26,34]

II. ALLOY DESIGN

The alloying elements such as C, Mn, Si, Mo, Cr, Ni and Al are generally used in the Q&P steels.[35–37] Carbon and Mn are austenite stabilizers[38] and are found to increase the resultant amount of retained austenite after the Q&P processing.[39,40] They are known to improve the hardenability of steel.[16] However, C and Mn cannot be added arbitrarily since they deteriorate the weldability.[41] Silicon is added to retard the cementite formation.[9,42–44] Even Al and P produce similar retardation effects on cementite formation but to a lower extent.[45] However, addition of Si deteriorates coatability.[46] Partial or full replacement of Si by Al improves the coatability[46,47] but it decreases the resultant amount of retained austenite after the Q&P process.[4] Nickel results in grain refinement and increases the stability of retained austenite after the Q&P process.[36,48] It also reduces the tendency of distortion and cracking during quenching. However, Ni is an expensive alloying element and thus should be added judiciously. Addition of Cr and Mo promotes austenite retention at room temperature (*RT*)[36,39,49] and decreases the sensitivity of the retained austenite fraction to the partitioning temperature and time.[36,39] Molybdenum is an expensive element and also forms complex carbides (when Mo is higher than 0.5 wt pct)[50] and is thus expected to decrease the solute carbon content of austenite. Chromium addition, on the other hand, results in a coarser austenite with interconnected network which is expected to be less stable.[51] Addition of Mo along with Al decreases the amount of retained austenite after the Q&P treatment and is found detrimental to the elongation.[39]

The influence of some of these alloying elements on various aspects of the Q&P process such as QT^{opt} and the corresponding amount of retained austenite, critical cooling rate (CCR) for martensite transformation, mechanical and thermal stability of austenite and cementite formation from austenite is estimated in this section. Thermodynamic software ThermoCalc and semi-empirical relations from literature[28–33] were used for the calculations. A base composition Fe–0.25C (wt pct) was used for these calculations. In order to understand the effect of individual alloying elements on various aspects, their concentration was varied keeping carbon constant at 0.25 wt pct.

A. *Optimum Quenching Temperature (QT^{opt})*

A simple model has been proposed by Speer *et al.*[52] to calculate the QT^{opt} and corresponding amount of retained austenite, assuming complete carbon partitioning from supersaturated martensite to untransformed austenite and complete suppression of the competing reactions. In these model calculations, the M_s temperature was calculated using Andrews empirical equation[30] (Eq. [1]) and the kinetics of martensite transformation during initial quenching before partitioning and final quenching after partitioning were predicted using Koistinen and Marburger (KM) equation[31] (Eq. [2]) as modified empirically by Van Bohemen[53] where the rate parameter (α_m) is not a constant at 0.011 but is calculated as a function of the alloy composition (Eq. [3]).

$$M_s(^{\circ}\mathrm{C}) = 539 - 423C_{\mathrm{C}} - 30.4C_{\mathrm{Mn}} - 12.1C_{\mathrm{Cr}} - 17.7C_{\mathrm{Ni}} - 7.583C_{\mathrm{Mo}} \quad [1]$$

$$f'_{\alpha} = 1 - \exp\left[-\alpha_m\left(M_s - T_Q\right)\right] \quad [2]$$

$$\alpha_m\left(\times 10^{-3}\mathrm{K}^{-1}\right) = 27.2 - 0.14C_{\mathrm{Mn}} - 0.21C_{\mathrm{Si}} - 0.11C_{\mathrm{Cr}} - 0.08C_{\mathrm{Ni}} - 0.05C_{\mathrm{Mo}} - 19.8[1 - \exp(-1.56C_{\mathrm{C}})] \quad [3]$$

where C_i is the concentration of element i in wt pct, $f_{\alpha'}^{o}$ is the fraction of martensite formed during initial quenching to T_Q which is below the M_s temperature. In the present investigation, $T_Q = QT$ during initial quenching and RT during the final cooling from PT to RT.

Figure 1 shows the results of the Speer model calculations for the base steel [Fe–0.25C (wt pct)]. The QT^{opt} is predicted to be 630 K (357 °C) corresponding to which 21 pct austenite is stabilized at RT (Figure 1).

Figures 2(a) through (d) shows the variation of the amount of retained austenite with QT for varying concentration of various alloying elements predicted using Speer's model. The QT^{opt} and the corresponding amount of retained austenite were then plotted with increasing contents of C, Mn, Ni and Cr and are shown in Figures 2(e) and (f), respectively. The QT^{opt} does not vary much for the lower carbon content (up to 0.10 wt pct) (Figure 2(e)). The QT^{opt} shifts to lower temperatures with an increase in the C (above 0.10 wt pct), Mn, Ni and Cr content while the corresponding amount of retained austenite increases with increasing concentration of C, Mn, Ni and Cr; among these, C has the largest effect (Figure 2(f)). From the industrial implementation point of view, the QT^{opt} should not be too low since a higher cooling rate is required to deep quench a bigger size sample which is difficult to achieve without using sophisticated cooling systems. Therefore, judicious selection of the alloying elements is necessary to ensure smooth processing.

Although some deviations between the experimental and predicted QT^{opt} and the corresponding amount of retained austenite were observed,[54,55] the variation of the amount of retained austenite, estimated using X-ray diffraction analysis was reported to be in qualitative agreement with the trends predicted using Speer's model.[9,25,56,57] Therefore, this model can be used to investigate the effect of alloying elements on the QT^{opt} and the corresponding amount of retained austenite. The deviations between the experimental and predicted results have been attributed to the violation of simplifying assumptions such as complete carbon partitioning, suppression of the carbide precipitation and bainite transformation during the partitioning treatment.[6,25,56,58]

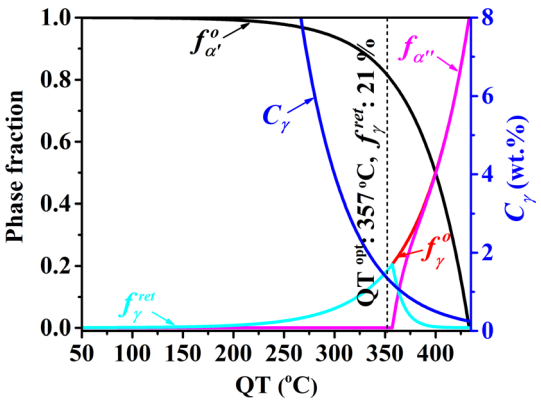

Fig. 1—The optimum quenching temperature (QT^{opt}) for the Fe-0.25 wt pct C steel using Speer's model. $f_{\alpha'}^{o}$: fraction of martensite formed during initial quench up to QT, f_{γ}^{o}: fraction of untransformed austenite at QT or in the beginning of partitioning, $f_{\alpha''}$: fraction of fresh martensite formed from carbon-enriched austenite during cooling from PT to RT, f_{γ}^{ret}: fraction of retained austenite in the final microstructure (at RT) and C_γ: carbon content of austenite remaining untransformed after partitioning.

B. *Critical Cooling Rate (CCR) for Martensite Transformation*

One of the major challenges for the industrial implementation of the Q&P processing is to ensure martensite transformation at relatively lower cooling rates so that additional more elaborate infrastructure for quenching is not require. The lower cooling rate reduces the risk of distortion and quench cracking which usually occur due to high thermal gradients associated with rapid cooling. In order to ensure martensite transformation at lower cooling rates, the steel should possess sufficient hardenability. The minimum cooling rate after austenitization that avoids all transformations other than martensite is referred to as critical cooling rate (CCR). The CCR is a measure of hardenability of the steel. A steel possessing high hardenability is the one which has a low CCR. Based on the statistical analysis of over 300 continuous cooling transformation (CCT) curves, Maynier *et al.*[29] proposed an empirical formula to predict the CCR for martensite transformation as a function of the alloy composition and austenitization condition for low-alloy steels with alloying elements less than 5 wt pct:

$$\mathrm{Log}_{10}(\mathrm{CCR}) = 9.81 - (4.62C_{\mathrm{C}} + 1.05C_{\mathrm{Mn}} + 0.54C_{\mathrm{Ni}} + 0.50C_{\mathrm{Cr}} + 0.66C_{\mathrm{Mo}} + 0.00183\mathrm{Pa}) \quad [4]$$

where CCR is in °C/h, C_i is the concentration of element i in wt pct, and Pa is the austenitization parameter which takes austenitization condition into account and can be expressed as:

$$\mathrm{Pa} = \left[\frac{1}{T_A} - \frac{nR}{H}\mathrm{Log}_{10}\frac{t}{t_o}\right]^{-1} \quad [5]$$

where T_A is the austenitization temperature in Kelvin, n is the Napierian logarithm of $10 \approx 2.3$, R is the universal gas constant, H is the activation energy for grain growth taken as 110 kcal mole^{-1}, t is the austenitization time and t_o is unit of time *i.e.* 1 hours.

Figure 3(a) shows the effect of different alloying elements on CCR calculated using Eqs. [4] and [5] assuming that the austenitization treatment was performed at 1223 K (950 °C) for 1 hour. The plain Fe–C and low-carbon low-alloy steels are not suitable candidates for Q&P processing since the CCR is quite high (Figure 3(a)), which is difficult to achieve during normal industrial practices. All the alloying elements considered here decrease the CCR and among these C and Mn have much pronounced effect (Figure 3(a)). Furthermore, an arbitrary steel of composition Fe–0.25C–1.5Mn–1.5Si–0.25Mo–0.5Ni (wt pct) is selected to investigate the effect of austenitization temperature (above A_{e3} temperature) on the CCR for martensite transformation and

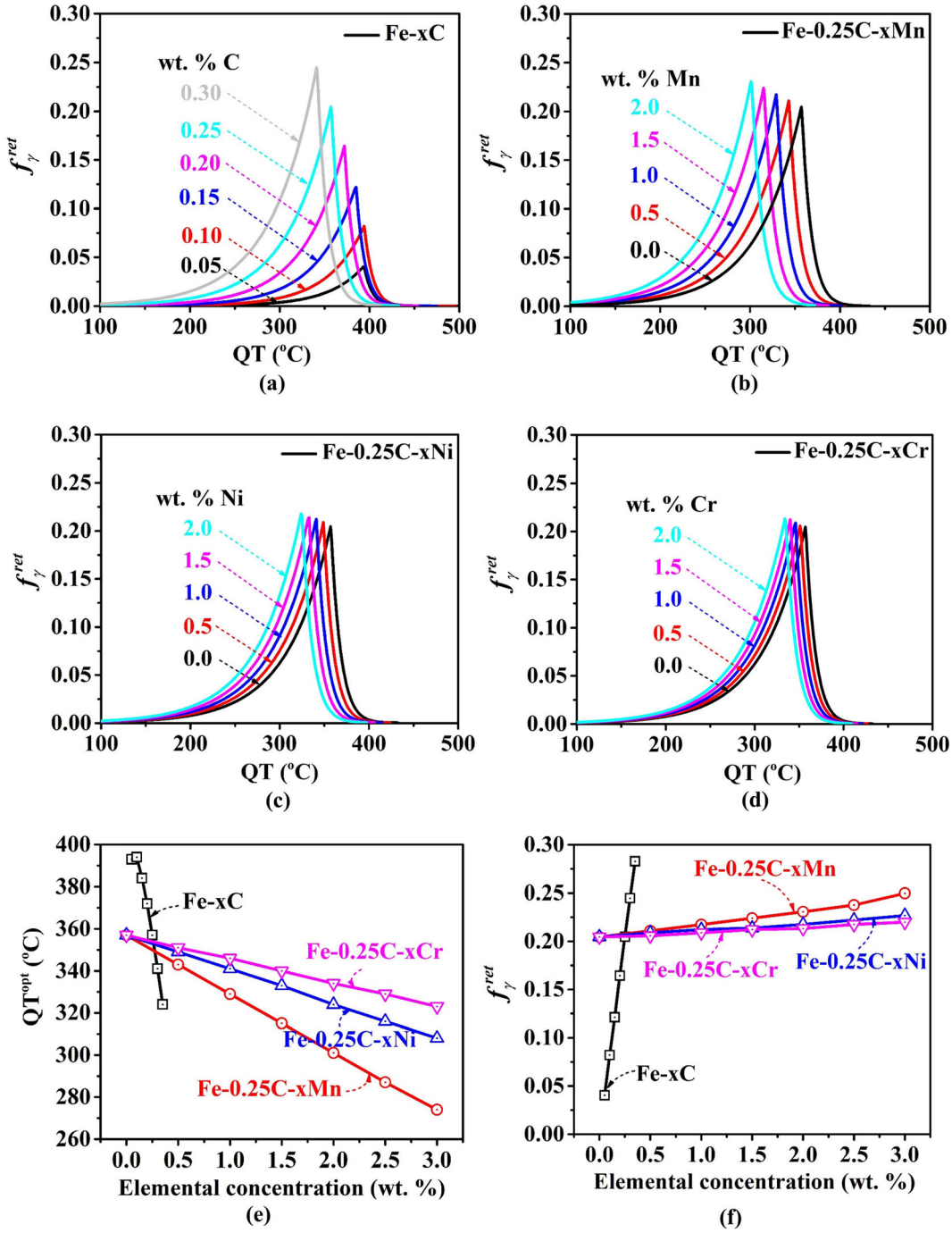

Fig. 2—Variation of the amount of retained austenite (f_γ^{ret}) with quenching temperature (QT) for various alloy compositions: (*a*) Fe–*x*C, (*b*) Fe–0.25C–*x*Mn, (*c*) Fe–0.25C–*x*Ni, (*d*) Fe–0.25C–*x*Cr and variation of (*e*) the optimum quenching temperature (QT^{opt}) and (*f*) corresponding f_γ^{ret}, as a function of the concentration of different alloying elements.

the calculation results are shown in Figure 3(b). These calculations indicate that the CCR decreases or hardenability increases with an increase in the austenitization temperature (Figure 3(b)) which is generally attributed to austenite grain coarsening so that the number of nucleation sites for ferrite and pearlite transformations decreases.[15] In a different study, Grange[16] showed that the hardenable diameter or hardenability varies linearly with the $d_\gamma^{-1/2}$, where d_γ is the mean austenite grain diameter.

It is important to note that, on one hand, smaller austenite grain size enhances the stability of retained austenite[59] while on the other, it hampers the hardenability of the steel.[16] These two opposing effects of austenite

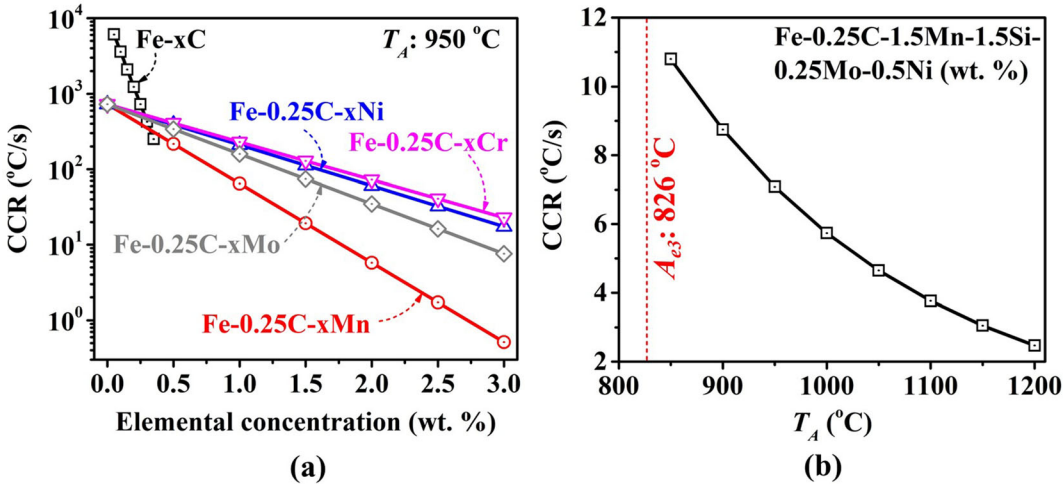

Fig. 3—The effect of the (*a*) various alloying elements on critical cooling rate (CCR) for martensite transformation assuming that the austenitization was done at 1223 K (950 °C) for 1 h and (*b*) austenitization temperature (T_A) on CCR of an arbitrary steel of chemical composition Fe–0.25C–1.5Mn–1.5Si–0.25Mo–0.5Ni (wt pct). The A_{e3} temperature of this composition was estimated using ThermoCalc with TCFE9 database.

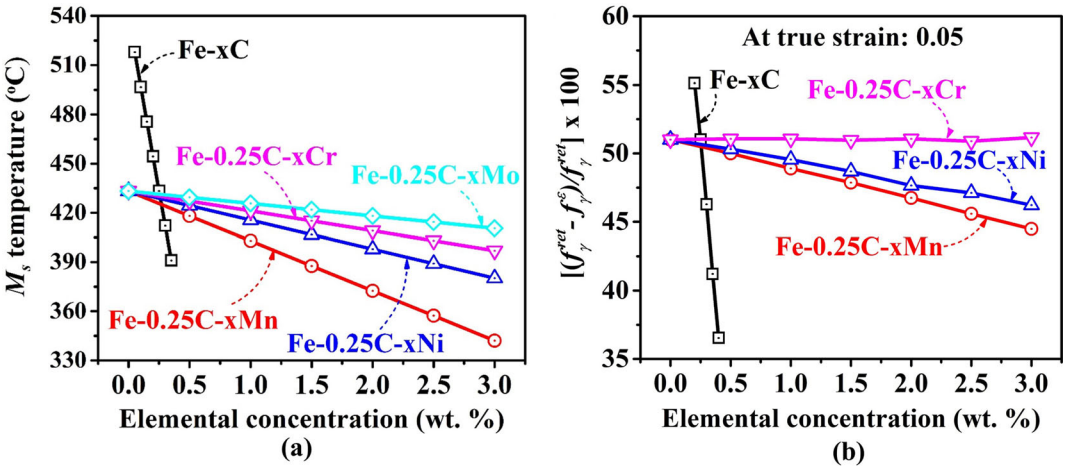

Fig. 4—Effect of various alloying elements on the (*a*) thermal and (*b*) mechanical stability of retained austenite.

grain size on the hardenability and the stability of austenite should be kept in mind while designing Q&P steel.

C. *Thermal and Mechanical Stability of Austenite*

The thermal stability of austenite against martensite transformation can be expressed in terms of the M_s temperature. A decrease in the M_s temperature indicates an increase in the thermal stability of austenite. The effect of various alloying elements on the M_s has been calculated using Andrews empirical formula[30] and is plotted in Figure 4(a). Addition of C, Mn, Ni, Cr and Mo enhances the thermal stability of austenite and among these C has the maximum effect (Figure 4(a)).

According to Sherif *et al.*,[33] anything that stabilizes austenite, for example, a higher amount of C, Mn, Ni, Cr and a higher deformation temperature make it more resistant against martensite transformation. Sherif *et al.*[33] have proposed a simple equation to express the mechanical stability of retained austenite against deformation-induced martensite transformation:

$$\ln f_\gamma^{\text{ret}} - \ln f_\gamma^{\varepsilon} = k_1 \Delta G^{\gamma-\alpha'} \varepsilon \qquad [6]$$

where f_γ^{ret} is the initial amount of retained austenite at zero strain, f_γ^{ε} is the fraction of retained austenite at a true strain of ε, k_1 is the proportionality constant whose value was deduced to be 0.00446 mol J^{-1} by Sherif *et al.*[33] and $\Delta G^{\gamma-\alpha'}$ is the free energy change for austenite to martensite transformation (of the same composition) at the deformation temperature. In order to study the effect of individual element on mechanical stability of retained austenite, it has been assumed that the sample is quenched to a QT at which ~ 70 pct martensite forms. The carbon content of austenite remaining untransformed after partitioning is then

calculated using carbon mass balance assuming complete carbon partitioning from martensite to untransformed austenite and no partitioning of substitutional alloying elements. The amount of retained austenite at RT after partitioning is then calculated using KM[31] and Van Bohemen[53] equations as already explained in Section II–A. The $\Delta G^{\gamma-\alpha'}$ values were calculated using ThermoCalc for the chemical composition of retained austenite at RT [298 K (25 °C)], the temperature of deformation. The extent of retained austenite transformation $\left(\frac{f_\gamma^{ret}-f_\gamma^e}{f_\gamma^{ret}}\times 100\right)$ at a true strain value of 0.05 was then calculated using Eq. [6] and is plotted in Figure 4(b) with varying concentration of the alloying elements studied here. It can be seen that the extent of retained austenite transformation to martensite decreases or mechanical stability of retained austenite increases with increasing concentration of C, Mn and Ni where C produces more pronounced effect. On the other hand, Cr does not have any significant effect on the mechanical stability of retained austenite (Figure 4(b)).

D. *Cementite Precipitation*

The formation of cementite from austenite becomes thermodynamically feasible when the carbon content of austenite exceeds the solubility limit given by extrapolated paraequilibrium $A_{CM}\left(A'_{CM}\right)$ line ($\gamma/(\gamma+\theta)$ phase boundary).[60,61] The maximum possible carbon enrichment of untransformed austenite $\left(C_\gamma^{max}\right)$ at a particular partitioning temperature (PT) can be given by constrained carbon equilibrium condition (CCE) as proposed by Speer *et al.*[1] to predict the end-point of carbon partitioning between primary martensite and untransformed austenite and explained schematically in Figure 5(a) for a Fe–C–M (M: substitutional element) system. At a critical partitioning temperature T_C, the value of C_γ^{max} is equal to the extrapolated A_{CM} carbon concentration in paraequilibrium condition $\left(C_\gamma^\theta\right)$ and therefore, cementite precipitation from austenite is not possible during partitioning at or above this temperature. If there is no kinetic hindrance, the formation of cementite from austenite would become possible below T_C since $C_\gamma^{max} > C_\gamma^\theta$. If addition of a particular alloying element shifts the extrapolated A_{CM} line to the right or C_γ^θ value increases then the cementite precipitation can be delayed to lower temperatures or in other words untransformed austenite can be enriched with carbon up to a greater extent without cementite precipitation.

The effect of different alloying elements on the C_γ^θ values was calculated using ThermoCalc and is plotted as a function of the composition at the PT of 673 K (400 °C) in Figure 5(b). Addition of Mn, Ni, Cr and Mo does not affect the C_γ^θ value much whereas Si dramatically increases the value and thus provides a wider window for carbon enrichment of austenite during partitioning without cementite precipitation (Figure 5(b)). Aluminum also produces similar effect but to a lower extent as compared with Si. It is noteworthy that the C_γ^{max} value, under the CCE condition, depends on the QT or the amount of primary martensite formed at QT $\left(f_{\alpha'}^o\right)$.[1]

In the calculations in Figure 5, the C_γ^{max} values under CCE condition as a function of PT for different $f_{\alpha'}^o$ values were calculated as discussed in various studies on the Q&P.[1,6,62,63] The effect of Si addition in base alloy on the $\left(C_\gamma^\theta - C_\gamma^{max}\right)$ values as a function of PT for the $f_{\alpha'}^o$ value of 0.80 is shown in Figure 5(c). It can be seen that Si shifts the T_C to the lower temperature and thus cementite precipitation become restricted. Furthermore, Figure 5(d) illustrates the effect of $f_{\alpha'}^o$ (or QT) on $\left(C_\gamma^\theta - C_\gamma^{max}\right)$ values at different PTs for the base alloy containing 1.5 wt pct Si. These results indicate that cementite precipitation is more likely to take place when the initial quenching temperature QT is lower, even if the steel is alloyed with high Si content.

In the Q&P steels, it is important to minimize the Si concentration since it deteriorates the coatability,[46] therefore these calculations are quite useful. In the above calculations, only thermodynamic aspect is discussed, however, it should be borne in mind that cementite precipitation depends on kinetics as well.[64]

Based on the detailed literature survey and calculations presented above, the range of alloying elements preferred for the Q&P steels is given in Table I.

III. EXPERIMENTAL PROCEDURES

A. *Alloy Preparation and Homogenization*

Based on the above discussions, a low-carbon low-alloy steel (alloying elements < 5 wt pct) was designed and melted using an air induction furnace. The chemical composition of the investigated steel is given in Table II. Laboratory scale melts of 5 to 10 kg were cast in the form of ingots. The as-cast ingot was homogenized at 1473 K (1200 °C) for 2 hours and then hot-forged to a final thickness of around 10 mm with a total reduction in thickness of 65 pct followed by normal air cooling. The different transformation temperatures of the designed steel are given in Table III. Solid cylindrical samples of 10 mm length and 4 mm diameter were fabricated from the as-forged material using wire EDM (electric discharge machining) cutting machine for dilatometry experiments. Small plates of thickness ~ 7 mm were also machined from the as-forged material to evaluate the mechanical properties after different heat treatments.

B. *Thermal Treatments*

Preliminary thermal treatments, shown schematically in Figure 6, were executed in a Bähr dilatometer (805 DIL A/D) having a resolution of 0.05 μm/0.05 °C. A Pt–Pt 10 pct Rh thermocouple was spot welded to the center of the samples for temperature measurement and control. The samples were cooled continuously from the austenitization temperature of 1223 K (950 °C) to room

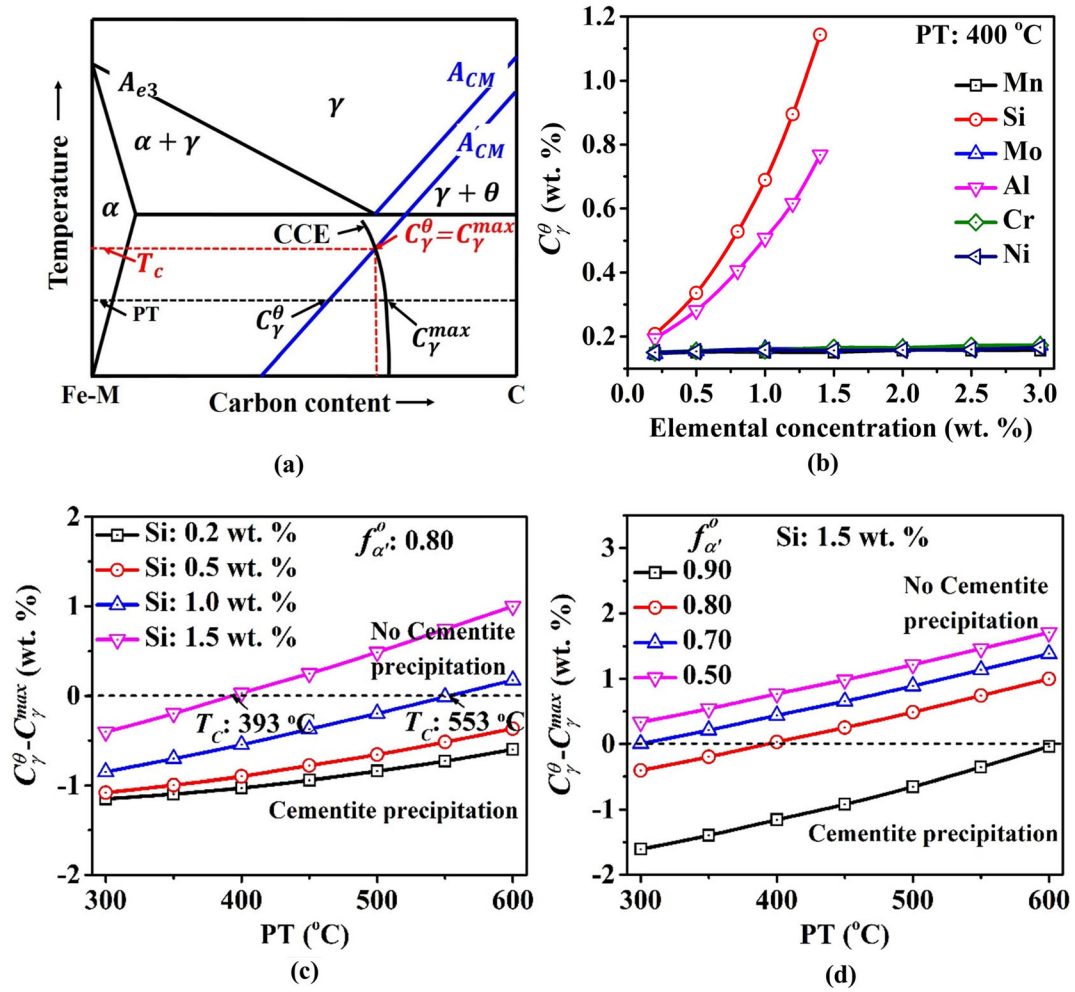

Fig. 5—(*a*) Schematic representation of the thermodynamic condition for cementite precipitation from austenite in a Fe–C–M system, where *M* represents substitutional alloying element and the effect of (*b*) various alloying elements on the extrapolated A_{CM} carbon concentration in paraequilibrium condition (C_γ^θ) at a partitioning temperature (*PT*) of 673 K (400 °C), (*c*) Si on ($C_\gamma^\theta - C_\gamma^{\max}$) values of the base alloy as a function of PT for the $f_{\alpha'}^o$ value of 0.80 and (*d*) $f_{\alpha'}^o$ on ($C_\gamma^\theta - C_\gamma^{\max}$) values of the base alloy consisting of 1.5 wt pct Si as a function of *PT*. $C_\gamma^{\max}$ is the maximum possible carbon enrichment of untransformed austenite that was calculated using CCE model for various *PT*s and $f_{\alpha'}^o$ is the amount of primary martensite formed during initial quenching to quenching temperature (*QT*). The calculations in (b) to (d) were performed using ThermoCalc.

temperature (*RT*) at cooling rates between 0.10 and 50 K/s (Figure 6(a)) to determine the transformation start and finish temperatures and continuous cooling transformation (CCT) diagram. The sample cooled at a cooling rate of 50 K/s to *RT* after austenitization at 1223 K (950 °C) is designated as the FQ sample (Figure 6(a)). Three dilatometry samples were subjected to isothermal bainite transformation (IBT) at 673 K, 623 K and 573 K (400 °C, 350 °C and 300 °C) after rapid cooling at 50 K/s from the austenitization temperature of 1223 K (950 °C). These samples were held at the respective temperatures until the bainite transformation reached stasis and were subsequently cooled to *RT* at a cooling rate of 50 K/s (Figure 6(b)). These thermal treatments are equivalent to the conventional austempering treatment and are designated as IBT400, IBT350 and IBT300. One additional sample was subjected to the Q&P treatment where after austenitization at 1223 K (950 °C) for 180 seconds, the sample was cooled rapidly to 533 K (260 °C) at a cooling rate of 50 K/s and held at that temperature for 2 seconds to homogenize the sample temperature. The sample was then heated rapidly to 673 K (400 °C) at 50 K/s and isothermally held at that temperature for 300 s for partitioning. After that, the sample was quenched to *RT* at 50 K/s (Figure 6(b)).

In addition to the above thermal treatments in the dilatometer on smaller samples, similar Q&P treatment was also performed on larger as-forged plates of dimensions 100 × 35 × 7 mm^3 in a salt-bath furnace to evaluate the tensile properties. The sample was austenitized at 1223 K (950 °C) for 30 minutes in a programmable muffle furnace. The sample was then quenched in a salt-bath furnace maintained at 533 K (260 °C) and held there for 30 seconds to homogenize the sample temperature. Subsequently the sample was transferred to another salt-bath furnace maintained at 673 K (400 °C) and held isothermally for 300 seconds

for partitioning before water quenching to *RT* (Figure 6(c)). The temperature of the molten salt was monitored using external thermocouples. For comparison purpose, the tensile properties of martensitic and bainitic microstructures of the investigated steel were also evaluated. To obtain the bainitic microstructure, the as-forged plate was austenitized at 1223 K (950 °C) for 30 minutes and then transferred to a salt-bath furnace maintained at 673 K (400 °C) where it was held isothermally for 30 minutes before finally quenching in water (Figure 6(c)). To obtain fully martensitic microstructure, the sample was directly water quenched to *RT* from the austenitization temperature of 1223 K (950 °C) (designated as WQ treatment), Figure 6(c).

C. *Metallographic Analysis*

A dilatometry sample was ground along the length, polished adequately followed by thermal etching in dilatometer[70] to reveal the prior austenite grain boundaries. This pre-polished sample was heated to 1223 K (950 °C) at 5 K/s, held at that temperature for 180 seconds in a high vacuum (10^{-5} mbar) and then continuously cooled to *RT* at 50 K/s, which is nothing but the FQ treatment (Figure 6(a)). The thermally etched sample was then observed under optical microscope. More than 500 grains were analyzed and their areas were converted to the equivalent circle diameter (ECD) grain sizes using the method described in Reference 71. The samples after thermal treatments in dilatometer (Figures 6(a) and (b)) were cut by slow-speed diamond cutting machine along the transverse direction in the centre, polished using standard polishing techniques and etched with 2 pct nital for metallography. The metallographic samples after the heat treatment in muffle and salt-bath furnaces were prepared from the through-thickness cross sections of the plates. The scanning electron microscopy (SEM) analysis was carried out on a Zeiss FESEM-MERLIN microscope.

D. *X-ray Diffraction Analysis*

X-ray diffraction experiments were performed on a Bruker D8 advance diffractometer using Co K_α radiation (wavelength: 1.789 Å) in a 2θ range of 45 to 130 deg with a step size of 0.02 deg. The fraction of retained austenite and the room temperature lattice parameters of retained austenite and martensite/bainitic-ferrite were estimated after analyzing the corresponding XRD peaks using the Rietveld refinement method.[72] The refinement method included the background, zero displacement, scale factors, unit cell parameters and temperature factors. The instrumental contribution to the line profile was also considered during the Rietveld refinement. The carbon contents of retained austenite $\left(C_\gamma^{\text{ret}}\right)$ and martensite/bainitic–ferrite $(C_{\alpha'})$ were estimated using empirical equations proposed by Dyson and Holmes[73] and Bhadeshia *et al.*,[74] respectively, assuming that the substitutional alloying elements do not partition during partitioning or IBT.[44,63,75,76] The dislocation density (ρ) of martensite/bainitic-ferrite was estimated from XRD data using Eq. [7],[77,78] as explained in Reference 34:

$$\rho = \frac{2\sqrt{3}\langle\omega^2\rangle^{1/2}}{Db} \qquad [7]$$

where D is the crystallite size, ω is the microstrain and b is the Burgers vector.

E. *Mechanical Testing*

The microhardness measurement on the samples thermally treated in the dilatometer was performed on UHL-VMHT 001 microhardness tester at 500 gmf load and 15 seconds dwell time. At least 6 readings were taken from different locations for each condition and their average is reported. Tensile test was done on the samples heat treated in salt-bath furnaces (Figure 6(c)) at a slow strain rate of 6.67×10^{-4} s^{-1} on Instron 8862 (100 kN) machine using standard sub-size flat samples (as per ASTM E8M standard) of gauge length 25 mm. The total length, width and the thickness of the tensile samples were 100, 10 and 4 mm, respectively. Strain was measured precisely by an external extensometer. For each heat treatment condition, at least two samples were tested. The strain hardening behavior of the heat treated samples during the tensile test was studied by analyzing the variation of the strain hardening rate $\left(\frac{d\sigma}{d\varepsilon}\right)$ with respect to the true strain (ε) between yield strength (YS) and tensile strength (UTS) (σ is the true stress).

IV. RESULTS AND DISCUSSION

A. *Continuous Cooling Transformation (CCT) Diagram*

The thermally etched microstructure showing the prior austenite grains at the austenitization temperature of 1223 K (950 °C) is given in Figure 7(a). The prior austenite grain size (PAGS) at 1223 K (950 °C) was measured to be 31 ± 6 μm from the corresponding thermally etched microstructures (Figure 7(a)), as explained in Section III–C. The distribution of PAGS at 1223 K (950 °C) is shown in Figure 7(b).

Typical dilatation curves and the corresponding SEM microstructures of the investigated steel at the cooling rates of 0.1, 2, and 10 K/s are shown in Figures 8(a) through (f). A small contraction in dilatation during heating has been observed in the temperature range of 504 °C to 577 °C (Figures 8(a), (c), and (e)) which is attributed to the carbide precipitation associated with the tempering of bainite present in the initial, as forged microstructure (Figure 14(a), Section IV–D).[79,80] The transformation temperatures during cooling were determined precisely by calculating the derivative of dilatation curves with respect to the temperature, as illustrated in Figures 8(a), (c) and (e). The experimental CCT curve of the investigated steel after austenitization at 1223 K (950 °C) is shown in Figure 8(g). As shown in Figure 8(b), a completely bainitic microstructure, including interlath film-like and blocky retained

Table I. Prescribed Range of Different Alloying Elements Commonly Used in Q&P Steels

Element	Effect	Prescribed Range (Wt Pct)	Higher Concentration
C	austenite stabilizer, decreases the CCR	0.20 to 0.30	deteriorates weldability,[41] increases the driving force for carbide formation[65, 66]
Mn	austenite stabilizer, decreases the CCR	< 2	deteriorates weldability, promotes banding
Si	retards cementite precipitation from austenite	< 1.5	deteriorates coatability[46]
Mo	decreases the sensitivity of retained austenite fraction to the partitioning time[67]	0.20 to 0.40	carbide formation[50], costly
Al	improves coatability	< 0.50	decreases the austenite retention at RT[4]
Cr	decreases the sensitivity of retained austenite fraction to the partitioning time, improves hardenability	< 1	carbide formation, coarse retained austenite[51]
Ni	grain refinement, increases the amount of retained austenite, decreases the tendency of distortion and quench cracking	< 1	costly
Co	promotes bainite transformation during partitioning treatment	not recommended	—
Nb, Ti, V	formation of microalloyed precipitates such as NbC	not recommended	—

Table II. Chemical Composition of the Designed Steel (Wt Pct) Measured Through Optical Emission Spectroscopy (OES)

C	Mn	Si	S	P	Al	Mo	Ni	Bal
0.24	1.87	1.31	0.008	0.03	0.34	0.32	0.66	Fe

austenite indicated by arrows, was obtained at the slowest investigated cooling rate of 0.1 K/s. The bainite transformation starts at 768 K (495 °C) at this cooling rate and it continues up to 591 K (318 °C) (Figure 8(a)). No other transformation was observed at this cooling rate (Figure 8(a)) and the hardness was measured to be the lowest (399 ± 11 HV0.5). The experimental B_s temperature is somewhat lower than the value calculated using the empirical equation proposed by Steven and Haynes[68] and a computer program MUCG83[69] (Table III). When the cooling rate was increased to 0.5 K/s, the bainite-start temperature decreased significantly to 658 K (385 °C) (Figure 8(g)). The transformation to bainite is accompanied by carbon enrichment of austenite[59,61,81] which subsequently transformed to martensite at 536 K (263 °C) (Figure 8(g)). The dilatation curve and the corresponding derivative curve at the cooling rate of 2 K/s in Figure 8(c) showed the occurrence of bainite and martensite transformation as confirmed by the corresponding SEM microstructure shown in Figure 8(d). Even at the cooling rate of 5 K/s, bainite transformation can be observed which is followed by the martensite transformation (Figure 8(g)). The formation of martensite leads to a significant increase in hardness from 399 ± 11 HV0.5 at 0.1 K/s to 511 ± 9 HV0.5 at 0.5 K/s. With an increase in the cooling rate above 0.5 K/s, the M_s temperature increases because of a decrease in the extent of carbon enrichment of austenite due to a smaller amount of bainite and then it remains almost constant at cooling rates higher than 10 K/s when bainite does not form. Though the amount of martensite increases with cooling rate and the amount of bainite decreases, its carbon content also decreases, which is why the hardness of the samples does not change much at cooling rates higher than 1 K/s (Figure 8(g)).

The microstructure and the dilatation curve at the cooling rate of 10 K/s indicates only the martensite transformation which starts at 611 K (338 °C) and continues up to 453 K (180 °C) (Figures 8(e) and (f)). In addition, the SEM microstructure of this sample also showed some transition carbide precipitates inside martensite laths (Figure 8(f)). The phenomenon of the formation of carbide precipitates during cooling is referred to as autotempering.[82] The formation of transition carbides during quenching has also been reported in other studies.[12,44,83] Furthermore, the hardness of this sample was measured to be 531 ± 5 HV0.5 which is close to the hardness of martensite in Fe-0.24 wt pct C alloys (550 HV).[84] The measured M_s is lower than the calculated values (Table III). This observed discrepancy in M_s may be because the Andrews empirical equation[30] applies to a specific range of composition. In addition, the measured M_s is reported to depend on PAGS[59,85–90] which is ignored in Andrews empirical formula.[30]

The CCR for the investigated steel is calculated to be 3.3 K/s using the empirical equation proposed by Maynier *et al.*[29] which is somewhat less than its experimental value of 10 K/s. The investigated steel contains Si and Al (Table II) whereas the empirical equation proposed by Maynier *et al.*[29] (Eq. [4]) does not consider the effect of these elements on CCR. Therefore, the observed discrepancy in CCR is because of the addition of Si and Al in the investigated steel since these elements are known to shift the time–temperature-transformation (TTT) diagram of ferrite to the left side[17] and hence they increase the CCR for martensite transformation.

It is quite interesting to observe that the room temperature length of the sample in the beginning of heating is higher than that at the end of the cooling cycle for the slowest cooling rate of 0.1 K/s whereas this difference decreases with an increase in the cooling rate (Figures 8(a), (c) and (e)). This is possibly due to a change in the product from bainite at the slowest cooling rate of 0.1 K/s to a mixture of bainite and martensite at 2 K/s and finally to martensite at the cooling rate of 10 K/s. However a more comprehensive analysis of these results is required to make any firm conclusion.

B. *Preliminary Phase Transformation: Quantification of the Q&P Microstructure*

During Q&P treatment, in general, martensite transformation takes place during initial quenching to the QT from the austenitization temperature whereas the formation of bainite occurs during partitioning. The formation of fresh martensite can also occur during final quenching from PT to RT, depending on the carbon concentration of untransformed austenite. Therefore, it is imperative to study the kinetics of martensite and bainite transformation separately for a better understanding of the evolution of microstructure during the Q&P process which are discussed in this section. The estimation of the amount of product phases from the resultant Q&P microstructure is somewhat complicated since primary martensite formed during initial quenching gets tempered during the partitioning treatment and, in most of the cases, it is difficult to distinguish it from bainite formed during partitioning. In this section, an alternate method involving analysis of dilatation data has also been discussed to quantify the multiphase Q&P microstructures.

1. *Kinetics of martensite transformation*

The kinetics of the martensite transformation was analyzed to estimate the amount of martensite formed during initial quenching to QT (which is below the M_s temperature). The experimental dilatation curve of the FQ sample, shown in Figure 9, was fitted to the calculated dilatation curve by varying the linear thermal expansion coefficient and phase fraction of martensite iteratively to obtain the best fit ($R^2 \sim 1$) as described by Ranjan and Singh.[91] Using this iterative method, the

Table III. Various Transformation Temperatures of the Designed Steel

Calculated [K (°C)]					
		M_s		B_s	
A_{e1}	A_{e3}	Andrews[30]	MUCG83[69]	Steven & Haynes[68]	MUCG83[69]
952 (679)	1109 (836)	640 (367)	642 (369)	819 (546)	794 (521)

While the A_{e1} and A_{e3} temperatures were calculated using ThermoCalc with TCFE9 database, the M_s (martensite-start) and B_s (bainite-start) temperatures were calculated using Andrews[30] and Steven and Haynes[68] empirical equations, respectively. The M_s and B_s temperatures were also calculated using a freely-available computer program MUCG83.[69]

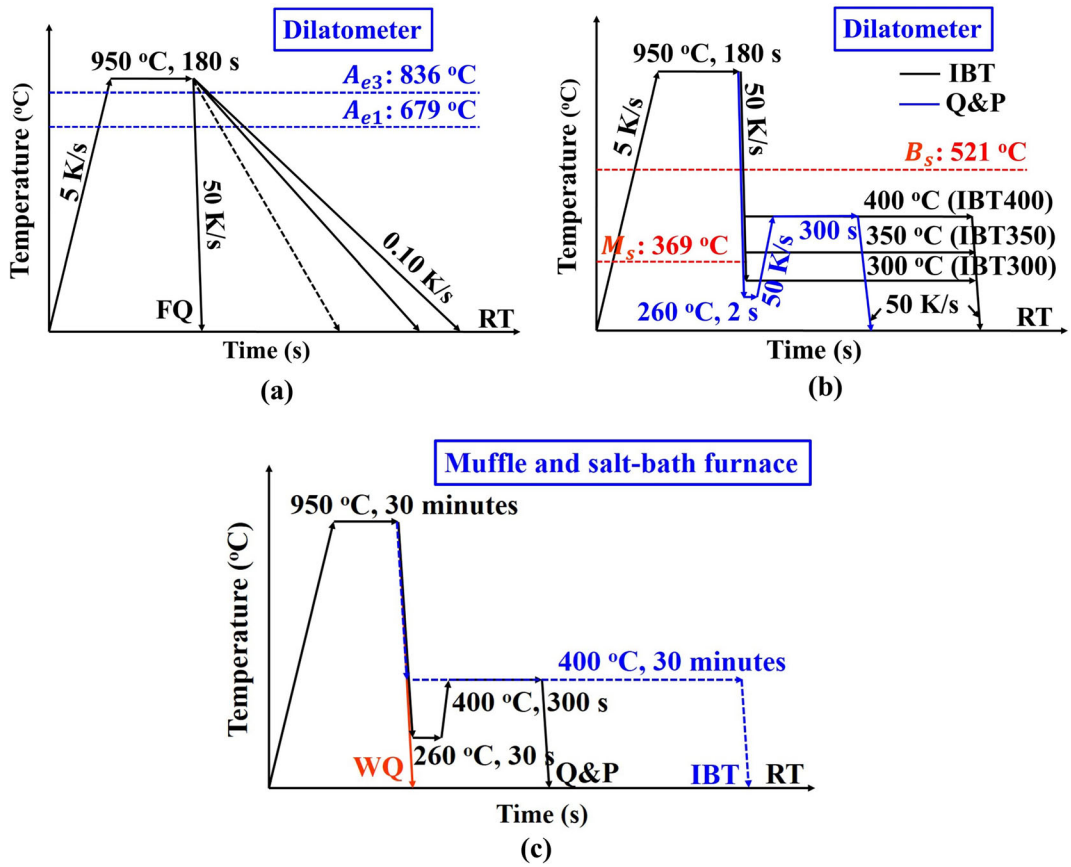

Fig. 6—Schematic representation of the thermal treatment: (*a*) simple heating–cooling cycles to determine the transformation start and finish temperatures and continuous cooling transformation (CCT) diagram, (*b*) IBT treatments at 673 K, 623 K and 573 K (400 °C, 350 °C and 300 °C), and Q&P treatment executed in dilatometer and (*c*) WQ, IBT400 and Q&P treatments performed in a muffle and salt-bath furnaces. The muffle furnace was used for the austenitization at 1223 K (950 °C) for 30 min. Salt-bath furnaces were used for quenching to 533 K (260 °C), partitioning and isothermal bainite transformation at 673 K (400 °C).

amount of primary martensite $\left(f_{\alpha'}^{o}\right)$ at the QTs of 298 K, 533 K and 573 K (25 °C (*RT*), 260 °C and 300 °C) was estimated to be 0.95, 0.81 and 0.49, respectively, as detailed in the previous work.[34]

2. *Kinetics of bainite transformation*

The dilatation curves obtained after the IBT treatments (Figure 6(b)) are shown in Figure 10(a). The dilatation curve of the Q&P sample from the previous work[34] is also included in Figure 10(a) for a direct comparison with IBT samples. The dilatation curves do not indicate any other transformation before isothermal holding at 673 K and 623 K (400 °C and 350 °C), whereas a sharp expansion before isothermal holding at 573 K (300 °C) indicates the formation of athermal martensite between M_s and 573 K (300 °C) (Figure 10(a)). Figure 10(b) shows the dilatation curves representing the isothermal bainite transformation kinetics during austempering treatments at 673 K, 623 K and 573 K (400 °C, 350 °C and 300 °C). The total relative change in length $\left(\frac{\Delta L}{L_o}\right)$ due to the bainite transformation at respective IBT and partitioning temperatures is also mentioned in Figure 10(b).

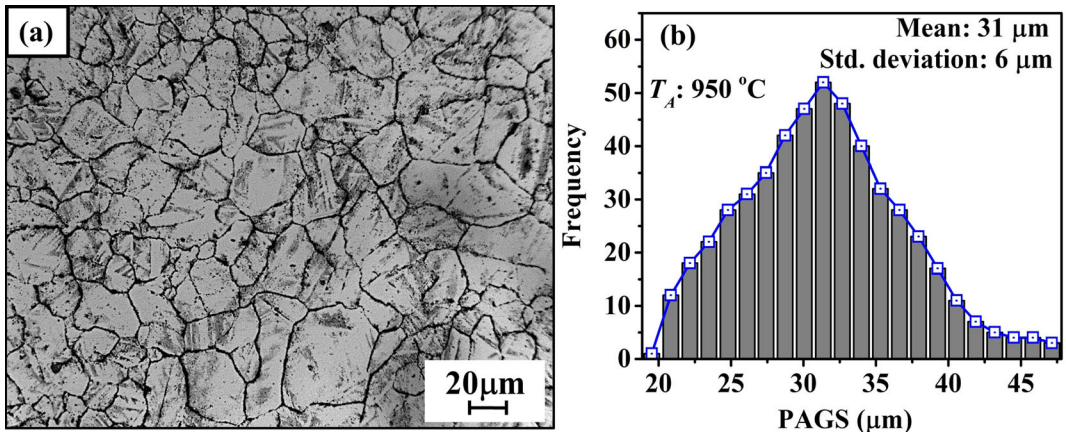

Fig. 7—(*a*) Optical microstructure showing prior austenite grains at 1223 K (950 °C) revealed by thermal etching technique and (*b*) distribution of prior austenite grain size (PAGS). T_A: austenitization temperature.

The $\frac{\Delta L}{L_o}$ value for bainite transformation at 623 K (350 °C) is somewhat higher than at 673 K (400 °C) (Figure 10(b)). This is obvious since the amount of bainite increases with decrease in the transformation temperature because of the increase in the driving force for the transformation.[61] However, since 49 pct austenite has already transformed to martensite during quenching to 573 K (300 °C), $\frac{\Delta L}{L_o}$ is the lowest in this case among the IBT treatments studied here. An acceleration in the kinetics of bainite transformation during the IBT treatment at 573 K (300 °C) is evident from a comparison of the dilatation curves at 573 K, 623 K and 673 K (300 °C, 350 °C and 400 °C) (Figure 10(b)). The observed acceleration in the kinetics of bainite transformation is ascribed to the formation of prior martensite that creates a large number of nucleation sites for bainite in the form of martensite/austenite interfaces.[92–94]

A small volume expansion is also observed in the Q&P sample during the partitioning treatment at 400 °C (Figure 10(b)). In related studies on the Q&P processing, a small positive dilatation was also reported during partitioning which was attributed to the bainite transformation.[10,12,25,55,95] The dilatation observed during the partitioning treatment at 673 K (400 °C) in the present case is quite small. This is because a significant amount of austenite (~ 81 pct), has already transformed to martensite during initial quenching to 533 K (260 °C) and thus only a small amount of bainite is expected to form during the partitioning treatment. However, if the sample is quenched to a higher QT (below the M_s), a higher amount of bainite is expected to form during the partitioning treatment.[12] As stated above, estimation of the amount of bainite from microstructural investigation is quite difficult since it resembles tempered martensite. Alternatively, the dilatation observed during the partitioning treatment, along with the dilatation obtained during the austempering process can be used to quantify the amount of bainite formed during partitioning, as explained below.

The amount of bainite formed during the partitioning treatment was estimated by comparing the dilatation data during the partitioning treatment with IBT data, following the method suggested by Bhadeshia and Edmonds.[96] If the IBT and partitioning treatment are performed at the same temperature and the effect of carbon enrichment of austenite on the dilatation is neglected, the amount of bainite during partitioning can be calculated as:

$$(f_{\alpha_b})_{Q\&P} = (f_{\alpha_b})_{\text{IBT}} \frac{\left(\frac{\Delta L}{L_o}\right)_{Q\&P}}{\left(\frac{\Delta L}{L_o}\right)_{\text{IBT}}} \quad [8]$$

where $(f_{\alpha_b})_{IBT}$ is the fraction of bainite formed during the IBT treatment and $\left(\frac{\Delta L}{L_o}\right)_{Q\&P}$ and $\left(\frac{\Delta L}{L_o}\right)_{\text{IBT}}$ represent the relative length change observed during partitioning and IBT treatments, respectively.

3. *Fresh martensite*

As stated above, the formation of high carbon fresh martensite can occur during cooling to RT after austempering and/or partitioning treatment due to insufficient carbon enrichment of untransformed austenite. For example, the dilatation curve of the Q&P sample during final cooling from 673 K (400 °C) to RT given in Figure 11 shows a small deviation from linearity, which points towards the formation of a small amount of fresh martensite.[92,94,97] The temperature at which this deviation from linearity starts is referred to as fresh martensite start temperature (M'_S). Van Bohemen and Hanlon[97] quantified this small amount of fresh martensite formed during cooling after austempering between 723 K and 623 K (450 °C and 350 °C) in a Fe–0.29C–2.39Mn–1.76Si (wt pct) steel by comparing the dilatation at RT in this case with the dilatation due to complete martensite transformation when the sample is quenched directly to RT. In this work, this method used by Van Bohemen and Hanlon[97] is represented by Eq. [9]:

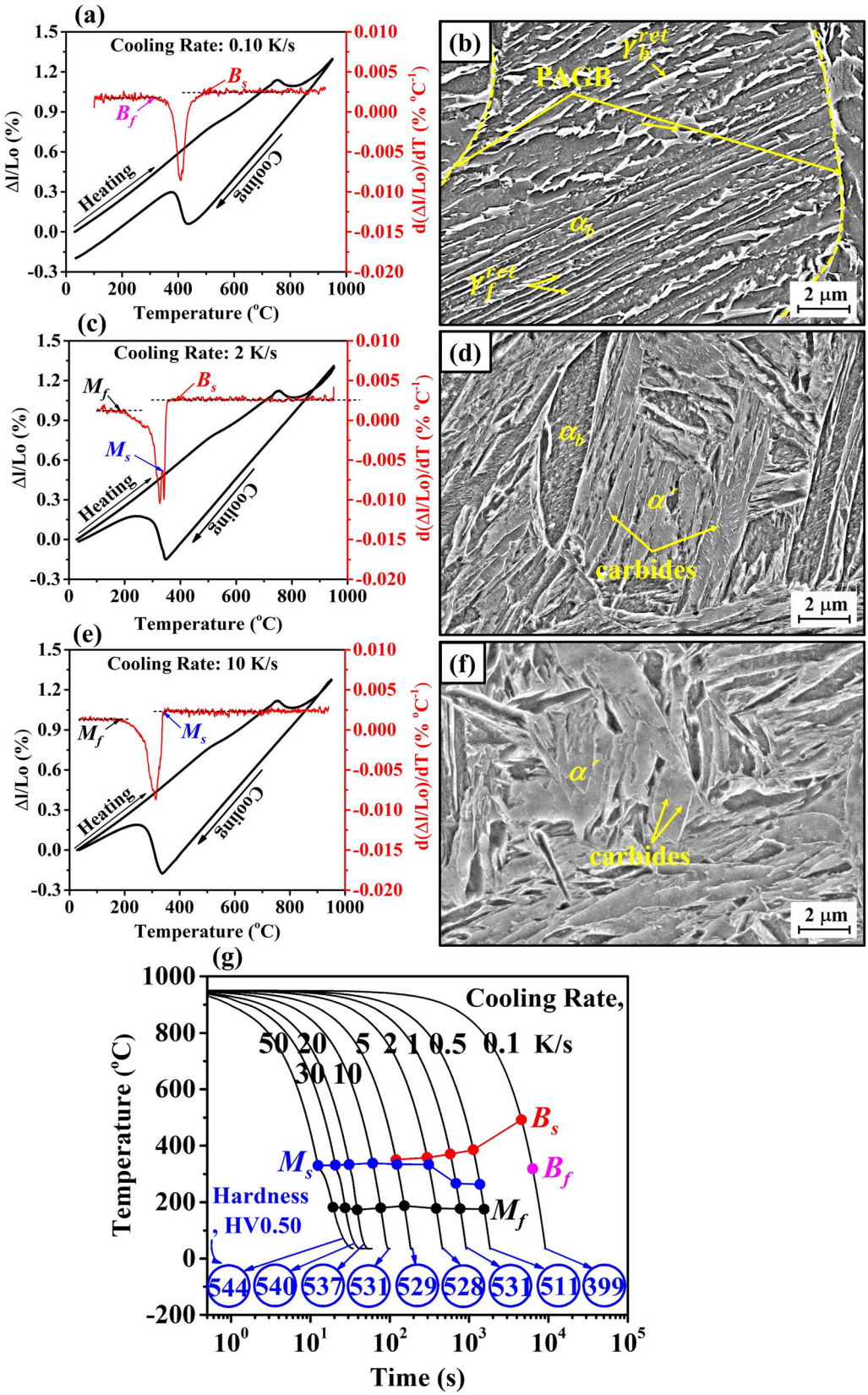

Fig. 8—Typical dilatation curves, along with their derivative with respect to temperature and the corresponding SEM microstructures at the cooling rates of (*a*) and (*b*) 0.1 K/s, (*c*) and (*d*) 2 K/s, (*e*) and (*f*) 10 K/s and (*g*) experimental CCT curve of the investigated steel determined using dilatometer, austenitization temperature: 1223 K (950 °C), prior austenite grain size (PAGS): 31 ± 6 μm.

$$(f_{\alpha''})_{\mathrm{IBT}/Q\&P} = (f^{o}_{\alpha'})_{FQ} \frac{\left(\frac{\Delta L}{L_o}\right)_{\mathrm{IBT}/Q\&P}}{\left(\frac{\Delta L}{L_o}\right)_{FQ}} \quad [9]$$

where $(f_{\alpha''})_{IBT/Q\&P}$ is the amount of fresh martensite formed after austempering or partitioning treatment and $(f^{o}_{\alpha'})_{\mathrm{FQ}}$ represents the amount of martensite formed at *RT* in a full quenched (FQ) sample which was estimated to be 0.95 by the iterative method discussed in Sect. IV–B. However, X-ray diffraction analysis showed no austenite peak for the FQ sample[34], since it is difficult to detect less than 5 pct austenite using X-ray diffraction experiment.[98] $\left(\frac{\Delta L}{L_o}\right)_{FQ}$ is the dilatation at *RT* obtained after full quenching and can be calculated as explained in Figure 11 (indicated by a double-ended arrow). $\left(\frac{\Delta L}{L_o}\right)_{IBT/Q\&P}$ is the dilatation at *RT* due to martensite transformation after the austempering or partitioning treatment and is indicated for the Q&P sample in Figure 11. A similar method has also been employed to quantify the amount of fresh martensite in other studies.[92,94] The amount of fresh martensite formed during quenching after austempering and partitioning treatments, both at 673 K (400 °C), is calculated to be ~ 3.1 and 2.3 pct, respectively using the method described above.

Finally, the amount of retained austenite at *RT* can be calculated by balancing the amounts of primary martensite, bainite and fresh martensite.

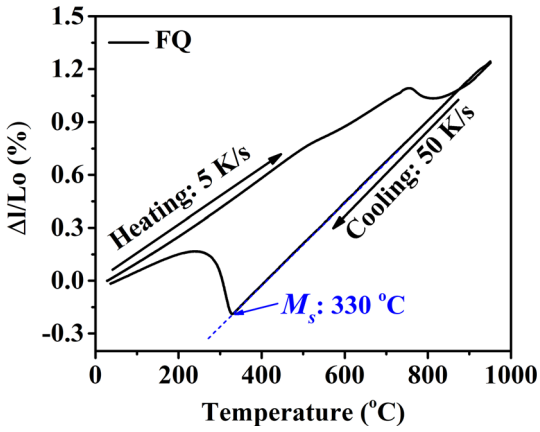

Fig. 9—Dilatation curve obtained after the FQ treatment.

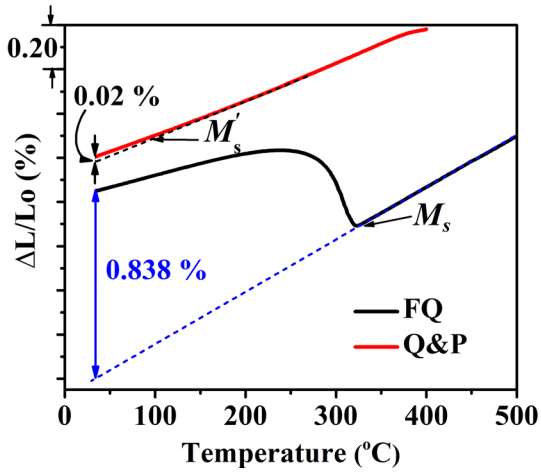

Fig. 11—Dilatation curves obtained during cooling after partitioning at 673 K (400 °C) (Q&P) and during FQ treatments. The dilatation at room temperature (298 K (25 °C)) due to martensite transformation is indicated by the double-ended arrows.

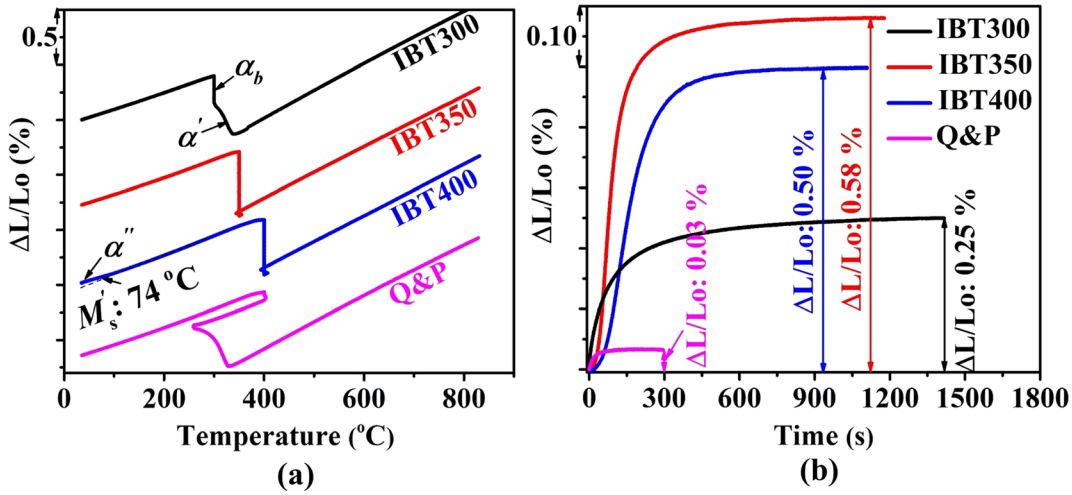

Fig. 10—(*a*) Dilatation curves obtained after the isothermal bainite transformation (IBT) at 673 K, 623 K and 573 K (400 °C, 350 °C and 300 °C), and Q&P treatment and (*b*) relative change in length vs. time plot during isothermal bainite transformation at 673 K, 623 K and 573 K (400 °C, 350 °C and 300 °C) and during partitioning at 673 K (400 °C) in the Q&P sample.

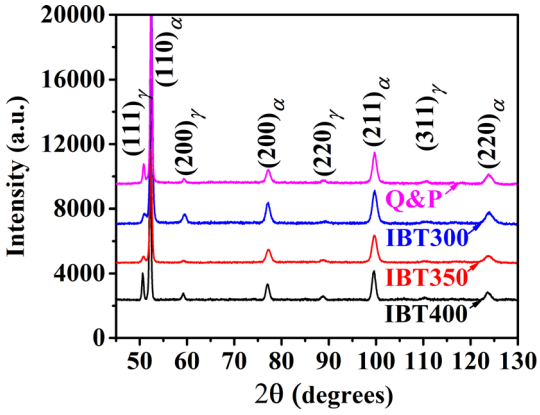

Fig. 12—X-ray diffraction patterns obtained after the IBT and Q&P treatments executed in dilatometer.

Table IV. Amount of Retained Austenite (f_γ^{ret}) and Its Carbon Content (C_γ^{ret}) of the Dilatometer Treated Samples as Estimated by the Rietveld Analysis[72] of the XRD Patterns

Thermal Treatment	f_γ^{ret}	C_γ^{ret}(Wt Pct)
IBT400	0.15 ± 0.002	1.01 ± 0.015
IBT350	0.08 ± 0.001	1.05 ± 0.022
IBT300	0.07 ± 0.001	0.86 ± 0.020
Q&P	0.12 ± 0.002	0.94 ± 0.011

C. *Estimation of the Amount of Retained Austenite and Its Carbon Content*

XRD patterns after the IBT and Q&P treatments carried out in the dilatometer are shown in Figure 12. The amount of retained austenite and its carbon content, estimated by the Rietveld analysis[72] of XRD data, are summarized in Table IV. Approximately 15, 8 and 7 pct retained austenite containing ~ 1.01, 1.05 and 0.86 wt pct carbon is estimated in the IBT400, IBT350 and IBT300 samples, respectively. By comparison, ~ 12 pct retained austenite with 0.94 wt pct carbon content has been reported after the Q&P treatment (Table IV).[34]

After the austempering treatment at 673 K (400 °C) (Figure 6(b)), the amount of fresh martensite is calculated to be 3.1 pct (Sect. IV–B, Eq. [9]) and retained austenite is estimated to be 15 pct (XRD), therefore, the rest ~ 82 pct is bainitic-ferrite. Using this result along with the $\frac{\Delta L}{L_o}$ values obtained during austempering and partitioning treatments at 673 K (400 °C) (Figure 10(b)), the amount of bainite formed during partitioning at 673 K (400 °C) is estimated to be 5.0 pct using Eq. [8]. In addition to bainitic-ferrite, the Q&P microstructure in the present case consists of 81 pct primary martensite, 2.3 pct fresh martensite and thus the balance 11.7 pct is retained austenite. The amount of retained austenite estimated in this way is quite close to its actual value estimated from X-ray diffraction analysis (Table IV).

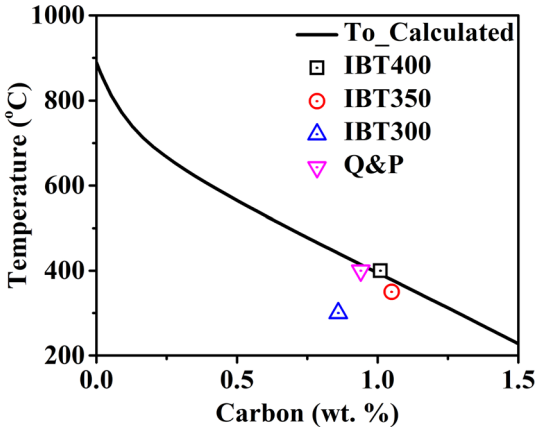

Fig. 13—T_0 Curve (black line) calculated using ThermoCalc and the experimental carbon content of retained austenite (symbols) estimated using XRD analysis for various thermal treatments executed in the dilatometer.

Figure 13 shows the T_0 curve of the investigated steel calculated using ThermoCalc along with the carbon content of retained austenite estimated experimentally from X-ray diffraction analysis. The estimated carbon contents of retained austenite after the IBT400 and IBT350 treatments are rather close to the T_0 curve. By contrast, the carbon concentration of the retained austenite in the IBT300 sample is much smaller than T_0 and also smaller than those in IBT400 and IBT350 samples. One of the possible reasons for this observation is as follows.

Due to higher carbon concentration of parent austenite and lower transformation temperature, the driving force for carbide formation increases[65,66] and thus formation of some carbide precipitates inside bainite is also possible which reduces the carbon enrichment of austenite. The microstructure described in the next section confirms this.

D. *Microstructure Evolution*

The SEM microstructures of the as-forged material is shown in Figure 14(a). The microstructure shows the presence of bainitic–ferrite along with interlath film-like retained austenite (γ_f^{ret}). The presence of some blocky austenitic (γ_b^{ret}) regions can also be seen in this microstructure. The SEM microstructure of the FQ sample shows lath martensite along with some tiny plate type carbides, Figure 14(b). Typical SEM microstructures obtained after the IBT400 and IBT300 treatments in dilatometer are shown in Figures 14(c) and (d), respectively. The microstructure of the IBT400 sample mainly consists of bainitic-ferrite along with film-like interlath austenite (Figure 14(c)). However, no carbide precipitates are observed in this microstructure. The presence of a small amount of fresh martensite can also be seen in this microstructure which correlates well with the corresponding dilatation data (Figure 10(a)), confirming the occurrence of the fresh martensite transformation during final cooling after the austempering treatment at 673 K (400 °C). The presence of martensite

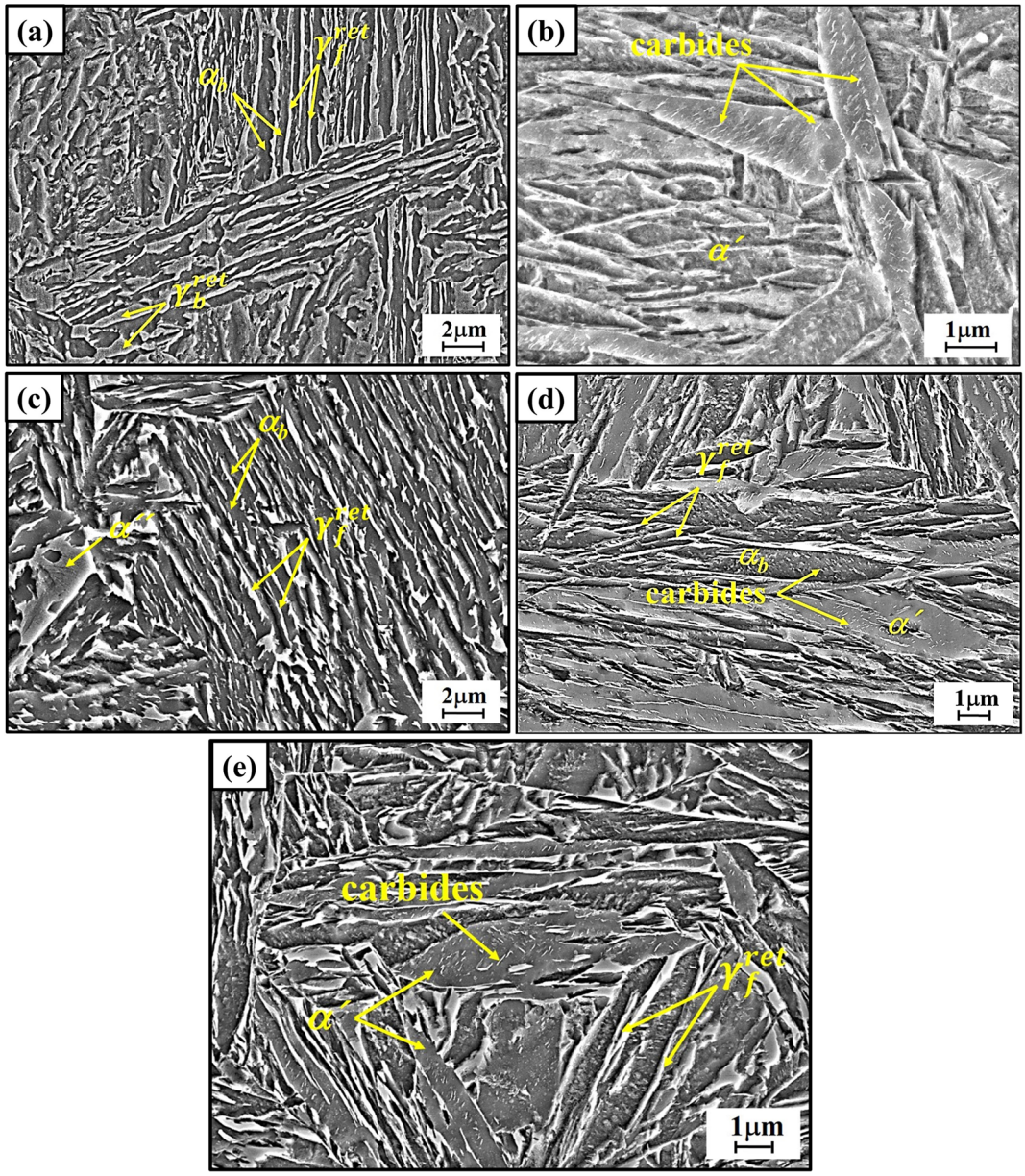

Fig. 14—SEM microstructure of the investigated steel after forging and various other thermal treatment in dilatometer as specified in Figs. 6(a) and (b): (*a*) the as-forged condition, (*b*) FQ, (*c*) IBT400, (*d*) IBT300 and (*e*) Q&P.α_b: bainitic-ferrite, γ_f^{ret}: film-like retained austenite and γ_b^{ret}: blocky austenite.

along with bainite can be seen in the sample isothermally transformed at 573 K (300 °C) (Figure 14(d)). Interestingly, some tiny carbides can be identified inside martensite and bainitic-ferrite in this sample which is one of the possible reasons for the lower T_0 carbon content of retained austenite (Figure 13), as explained in Section IV–C. The SEM microstructure of the Q&P sample that was initially quenched to 533 K (260 °C) and subsequently partitioned at 673 K (400 °C) for 300 seconds in dilatometer is also shown in Figure 14(e). The microstructure shows lath martensite and interlath film-like retained austenite, along with some plate type carbide within martensitic laths. Since the amount of bainitic-ferrite is very small (5 pct, as described above), it is not distinctly visible in this microstructure. It is noteworthy that Si is ineffective in suppressing the formation of carbide precipitates during IBT below M_s and Q&P treatments. The presence of transition carbide precipitates has also been observed in various other studies on the Q&P steels containing high Si (~ 1.5 wt pct).[7–9]

In order to analyze the microstructures further, the IBT400 and IBT300 samples were subjected to TEM investigations and the corresponding micrographs are shown in Figure 15. After isothermal transformation at 673 K (400 °C), the microstructure consists of bainitic-ferrite and films of austenite (Figure 15(a)). However, the carbide precipitates are not observed clearly. The microstructure of the IBT300 sample, on the other hands, consists of bainitic-ferrite along with

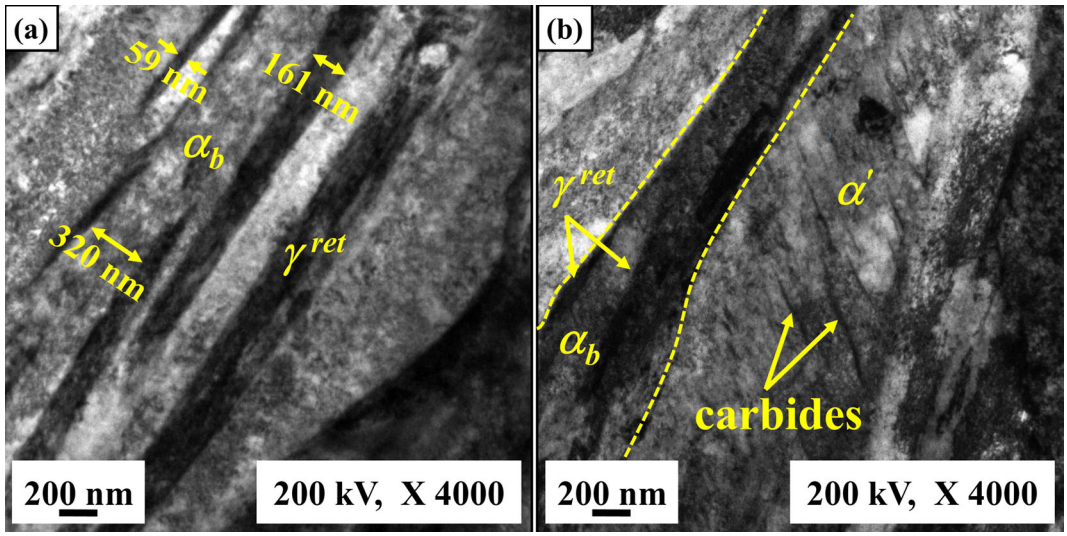

Fig. 15—Bright field TEM micrographs after thermal treatment in the dilatometer: (*a*) IBT400 and (*b*) IBT300 samples.

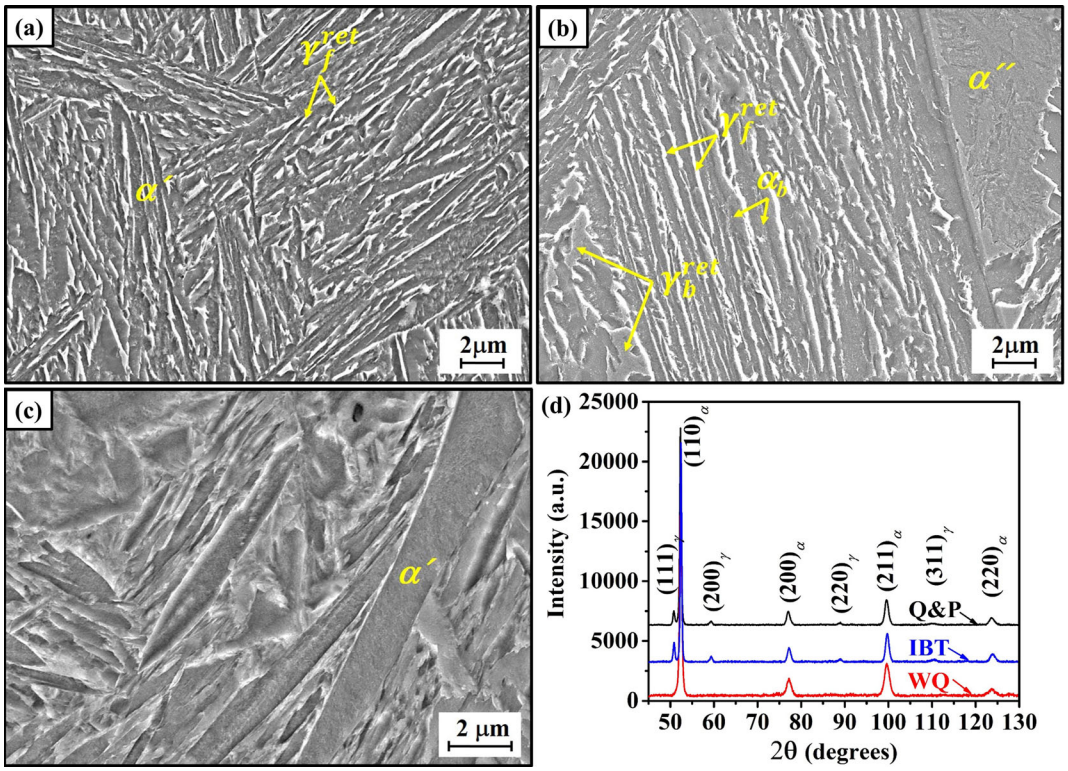

Fig. 16—SEM microstructure of the samples heat treated in muffle and salt-bath furnace: (*a*) Q&P, (*b*) IBT400, (*c*) WQ treatments and (*d*) XRD patterns of the Q&P, IBT400 and WQ samples.

laths of martensite containing of carbide precipitates. It is interesting to observe that the thickness of the bainitic plates in the IBT300 sample is smaller than in the IBT400 sample (Figure 15) which is also reflected by the corresponding SEM micrographs (Figures 14(c) and (d)). This is because the primary martensite formed during initial quenching (in the IBT300 sample) divides the untransformed austenite into smaller regions and thus bainite formed afterwards, during partitioning, also gets refined. Additionally, bainite in the IBT300 sample formed from high carbon austenite because of its enrichment as a result of the decarburization of primary martensite formed during quenching to 300 °C. This would have the effect of refining the bainitic-ferrite laths.[99]

The SEM microstructures of samples obtained after the Q&P, IBT400 and WQ treatments in muffle and salt-bath furnace are shown, respectively, in Figures 16(a) through (c) and the corresponding X-ray diffraction patterns are shown in Figure 16(d). The Q&P microstructure mainly consists of lath martensite along with film-like retained austenite (Figure 16(a)). As expected, the microstructure is predominantly bainitic in the IBT400 sample and martensitic in the WQ sample, Figures 16(b) and (c), respectively. The X-ray diffraction analysis showed around 9.3 pct retained austenite containing 1.02 wt pct carbon after the Q&P treatment and 12.8 pct retained austenite having 1.11 wt pct carbon after the IBT treatment while retained austenite was not detected in the WQ sample.

E. *Optimum Quenching Temperature: Speer's Model*

The optimum quenching temperature (QT^{opt}) for the investigated steel has been calculated using Speer's model[52] as explained in Section II–A and the results are shown in Figure 17. The QT^{opt} and the corresponding amount of retained austenite are calculated to be 294 °C and 23 pct respectively. However, the amount of retained austenite estimated using XRD analysis indicated the actual QT^{opt} of the investigated steel was 260 °C corresponding to which 12 pct retained austenite was obtained.[34] Therefore, a significant deviation between the actual and predicted QT^{opt} is evident and the primary reasons for these deviations are listed below:

(i) Incomplete carbon partitioning from martensite[34] and segregation of carbon atoms at dislocations.[34,100,101]
(ii) The empirical equation does not predict the kinetics of martensite transformation accurately.[26,34,55]
(iii) Carbide precipitation inside martensite (Figure 14(e)).
(iv) Bainite transformation during partitioning (Figure 10(b)).

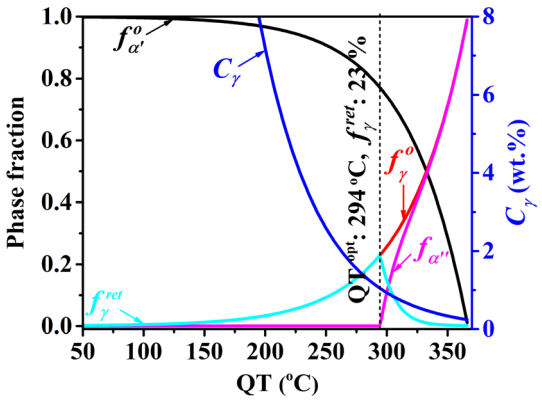

Fig. 17—Calculation of the optimum quenching temperature (QT^{opt}) for the investigated steel using Speer's model. The symbols used here have already been defined.

In the previous work of the present authors, Speer's model was revised, for the first time, after incorporating these factors.[34] The revised model showed a good agreement between the experimental and predicted QT^{opt} and the corresponding amount of retained austenite.[34]

F. *Mechanical Properties*

The engineering stress–strain curves after salt-bath heat treatments are shown in Figure 18(a) and corresponding tensile properties are tabulated in Table V. The Q&P treatment resulted in better mechanical properties compared with the WQ and IBT samples. It is important to note that the uniform elongation of the Q&P sample is slightly higher than the IBT sample even though the tensile strength of the Q&P sample is significantly higher (Table V). Furthermore, the highest UTS × TE value after the Q&P treatment (Figure 18(b)) signifies a more effective exploitation of the TRIP effect in this case[102,103] even though the Q&P sample contains a lower amount of retained austenite compared with the IBT sample.

In the case of the multi-phase microstructures, the stability of retained austenite or TRIP behavior depends not only on the amount of retained austenite and its carbon content but also on its morphology[19,104,105] and the stress/strain partitioning between austenite and the surrounding phases, which is also referred to as the composite effect.[19,106–108] The overall refinement of the resultant microstructure including retained austenite is evident after the Q&P processing as compared to the IBT sample (Figures 14 and 16). It has been argued that the deformation-induced transformation of austenite to martensite results in volume expansion, thereby, the surrounding matrix needs to deform plastically to accommodate this volume expansion.[19] In the present case, the matrix phase is decarburized martensite and bainitic–ferrite after the Q&P and IBT treatments in the salt-bath furnace, respectively. The carbon content of the decarburized martensite and bainitic-ferrite was estimated to be 0.04 and 0.02 wt pct, respectively, after analyzing the XRD data. The dislocation density of martensite and bainite, estimated from X-ray diffraction analysis using the method described in Section III–D (Eq. [7]), is summarized in Table VI. The dislocation density of martensite and bainite was estimated to be 5.45×10^{15} and 4.12×10^{15} m^{-2}, respectively (Table VI). These subtle differences are believed to be responsible for the higher yield strength (YS) of the Q&P sample than the IBT400 sample (Table V). It has been reported that 1 wt pct carbon in solution in ferrite increases the yield strength by about 4600 MPa and UTS by about 6800 MPa.[109,110] A 0.02 wt pct difference in the ferrite carbon concentration of Q&P and IBT sample would translate into a difference of 92 MPa in YS and 136 MPa in UTS. The observed difference is larger than this and points towards other possible mechanisms, like the ferrite plate size, the composite effect, the dislocation density and the TRIP effect, which need to be explored further. In the case of the Q&P treatment, the higher YS of the decarburized martensite

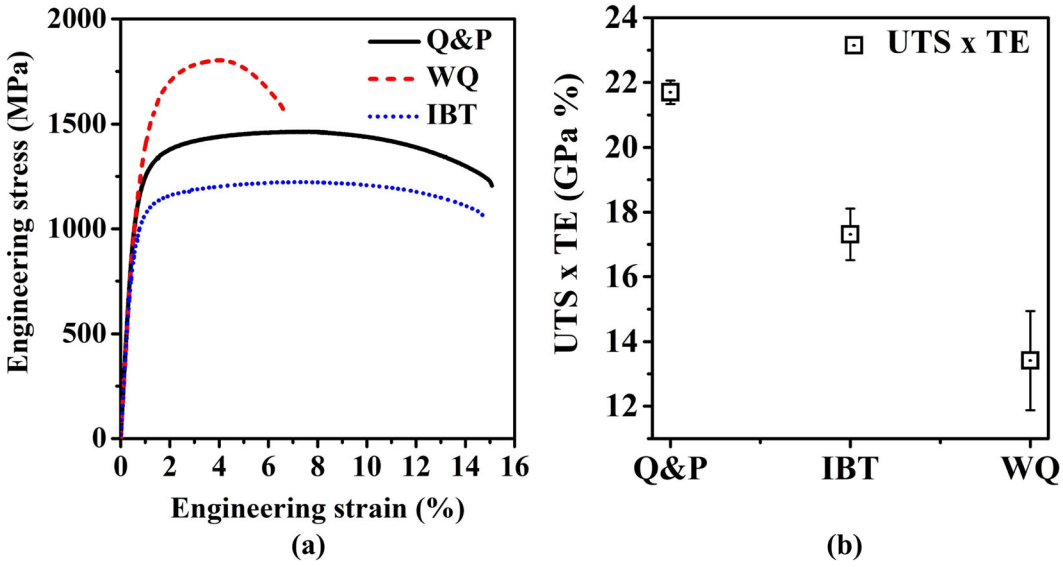

Fig. 18—Engineering stress–strain curves (*a*) and variation of the UTS × TE values (*b*).

Table V. Tensile Properties of the Investigated Steel After the Q&P, IBT400 and WQ Treatments

Heat Treatment	YS (MPa)	UTS (MPa)	TE (Pct)	UE (Pct)	UTS x TE (GPa Pct)
Q&P	1127 ± 5	1457 ± 7	14.9 ± 0.2	7.8 ± 0.4	21.7 ± 0.4
IBT400	964 ± 14	1222 ± 2	14.2 ± 0.6	7.1 ± 0.8	17.3 ± 0.8
WQ	1297 ± 7	1809 ± 7	7.4 ± 0.8	4.6 ± 0.4	13.4 ± 1.5

YS yield strength, *UTS* tensile strength, *TE* total elongation, *UE* uniform elongation.

Table VI. The Dislocation Density in Martensite and Bainite Estimated from the X-ray Diffraction Analysis

Heat Treatment	Dislocation Density ($\times 10^{15}$ m^{-2})
Q&P	5.45
IBT400	4.12
WQ	9.87

delays the onset of deformation-induced martensite transformation up to a higher strain,[19] thereby resulting in a more pronounced TRIP effect compared with the IBT sample.

The work hardening rate $\left(\frac{d\sigma}{d\varepsilon}\right)$ and true stress (σ) with respect to the true strain (ε) for the WQ, Q&P and IBT samples are shown in Figures 19(a) through (c), respectively. In the case of the WQ sample, the initial work hardening rate is much higher than the Q&P and IBT samples. This is due to the fact that the dislocation density of martensite in the WQ sample is higher than that in decarburized martensite and bainitic-ferrite in Q&P and IBT samples, respectively (Table VI). After an initial rapid decrease, the work hardening rate of the Q&P and IBT samples shows a gradual decrease with true strain at intermediate strain levels before attaining a near-constant value at higher strains because of additional strain hardening as a result of deformation-induced austenite to martensite transformation (Figures 19(b) and (c)). The WQ sample on the other hand shows a continuous but more rapid decrease of the strain hardening rate at all strains (Figure 19(a)). A comparison of the mechanical properties obtained after the Q&P treatment with the values reported by De Moor *et al.*[24,39] and Seo *et al.*[111] in Figure 20 shows encouraging results. Further work is however required to understand the effect of Q&P processing parameters on the mechanical properties.

V. CONCLUSION

In this work, some important alloy design aspects of Q&P steel have been discussed. A new low-carbon low-alloy steel has been designed and prepared in laboratory. Following are the important conclusions from the present investigation:

- The experimental CCT curve showed bainite transformation at the slowest investigated cooling rate of 0.1 K/s, bainite and martensite transformation at intermediate cooling rates between 0.5 and 5 K/s and only martensite transformation at or above the cooling rate of 10 K/s. The experimental critical cooling rate (CCR) for martensite transformation is found to be slightly higher than the value predicted using Maynier's empirical relationship.[29] This

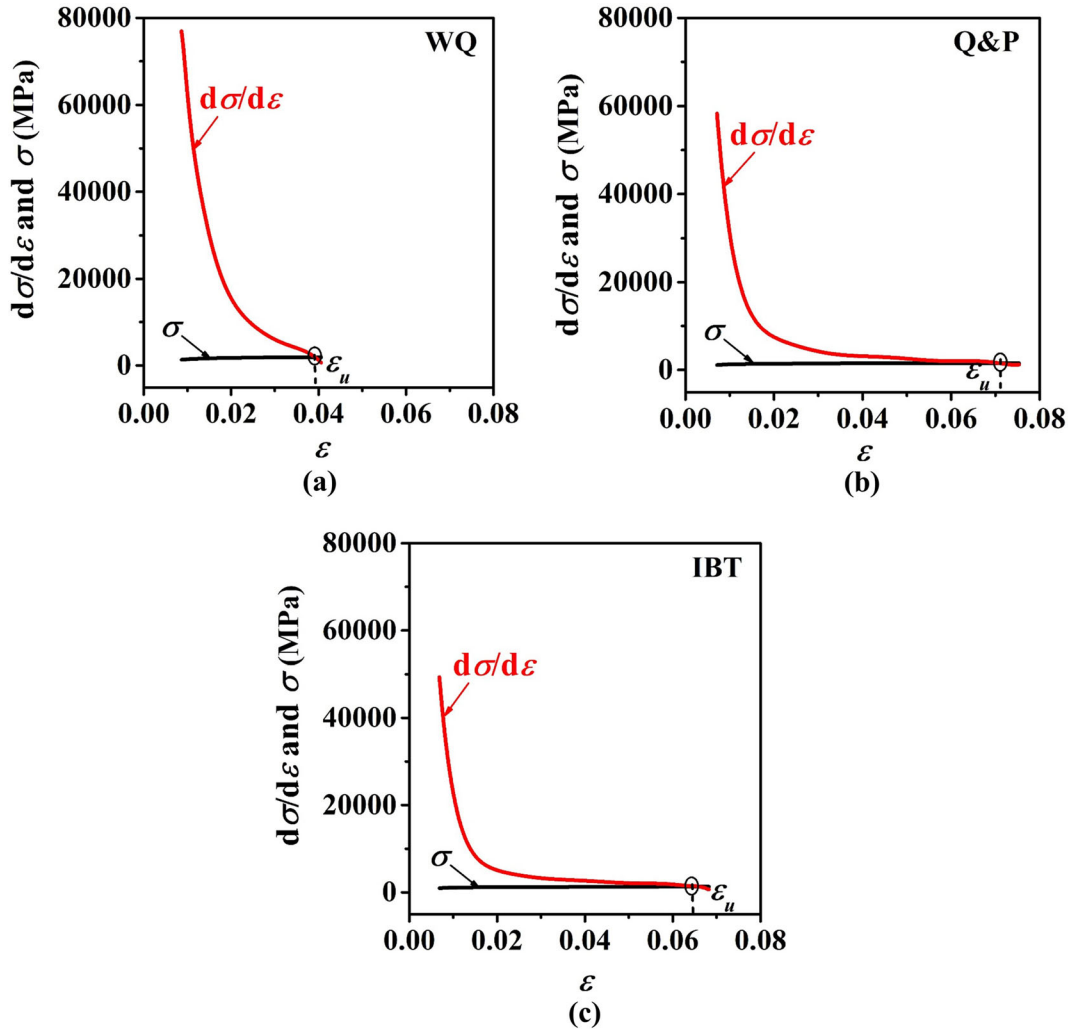

Fig. 19—Variation of the work hardening rate $\left(\frac{d\sigma}{d\varepsilon}\right)$ and true stress (σ) as a function of true strain (ε) for the (*a*) WQ, (*b*) Q&P and (*c*) IBT400 samples. ε_u true uniform elongation.

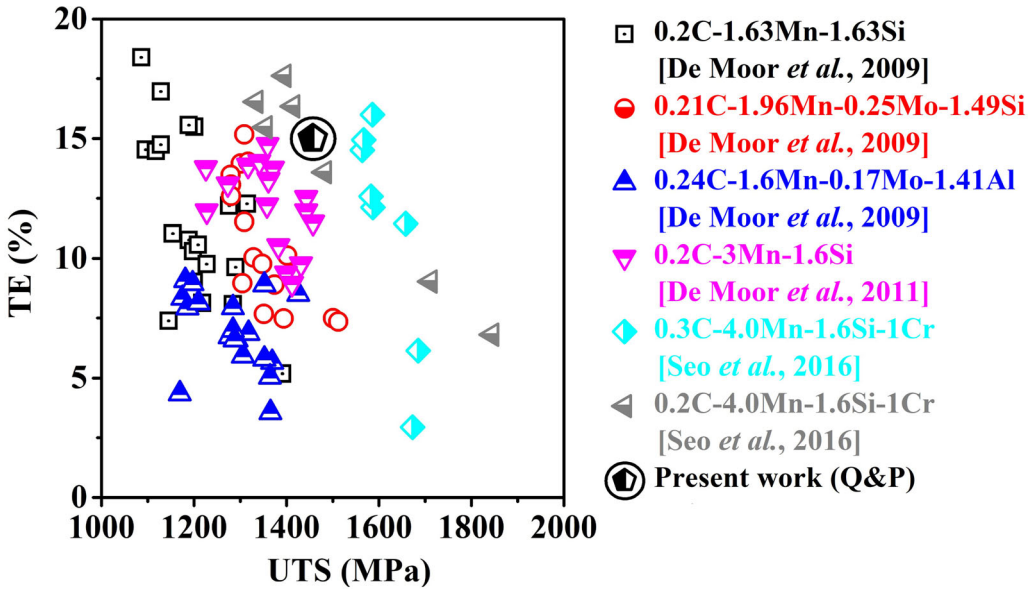

Fig. 20—Comparison of the mechanical properties obtained after the Q&P treatment with the literature data.[24,39,111]

deviation has been attributed to the presence of Si and Al in the investigated steel.

- The bainite-start temperature decreased with an increase in the cooling rate above 0.5 K/s, while the M_s temperature increased. The latter was attributed to the smaller extent of carbon enrichment of untransformed austenite because of a smaller amount of bainite.
- The microstructure of the sample thermally treated in the dilatometer showed autotempered carbide precipitates inside martensite laths in full quenched condition. The microstructure after austempering above M_s consisted of bainitic-ferrite with films of retained austenite whereas the microstructure after austempering treatment below the M_s consisted of martensite, bainite and retained austenite along with tiny carbide precipitates inside martensite and bainite both. The Q&P microstructure comprised decarburized martensite and film-like retained austenite.
- An alternative method to quantify the Q&P microstructure using the dilatation data has been proposed. It provided a close estimate of the actual amount of retained austenite stabilized at room temperature.
- The Q&P treatment resulted in better mechanical properties compared with martensitic and bainitic microstructures. The tensile strength (UTS) values of around 1.5 GPa with total elongation (TE) of around 15 pct has been obtained after the Q&P treatment. The strain hardening rate was found to decrease rapidly at lower strains and then it attained nearly a constant value at larger strains due to the TRIP effect.

ACKNOWLEDGMENTS

The authors gratefully acknowledge the Indian Institute of Technology Kharagpur for financial support. The authors are thankful to the Head of the Department of Metallurgical and Materials Engineering, IIT Kharagpur, for providing various research facilities.

CONFLICT OF INTEREST

On behalf of all authors, the corresponding author states that there is no conflict of interest.

REFERENCES

1. J. Speer, D.K. Matlock, B.C. De Cooman, and J.G. Schroth: *Acta Mater*., 2003, vol. 51, pp. 2611–22.
2. D.K. Matlock, V.E. Brautigam, and J.G. Speer: *Mater. Sci. Forum*, 2003, vol. 426–432, pp. 1089–94.
3. F. HajyAkbary, J. Sietsma, G. Miyamoto, N. Kamikawa, R.H. Petrov, T. Furuhara, and M.J. Santofimia: *Mater. Sci. Eng. A*, 2016, vol. 677, pp. 505–14.
4. E. De Moor, S. Lacroix, A.J. Clarke, J. Penning, and J.G. Speer: *Metall. Mater. Trans. A*, 2008, vol. 39A, pp. 2586–95.
5. D.K. Matlock and J.G. Speer: in *Proc. of the 3rd International Conference on Advanced Structural Steels*, Korean Institute of Metals and Materials, Seoul, South Korea, 2006, pp. 774–81.
6. J.G. Speer, D.V. Edmonds, F.C. Rizzo, and D.K. Matlock: *Curr. Opin. Solid State Mater. Sci.*, 2004, vol. 8, pp. 219–37.
7. D.T. Pierce, D.R. Coughlin, D.L. Williamson, J. Kähkönen, A.J. Clarke, K.D. Clarke, J.G. Speer, and E. De Moor: *Scr. Mater*., 2016, vol. 121, pp. 5–9.
8. S. Yan, X. Liu, W.J. Liu, H. Lan, and H. Wu: *Mater. Sci. Eng. A*, 2015, vol. 620, pp. 58–66.
9. D.V. Edmonds, K. He, F.C. Rizzo, B.C. De Cooman, D.K. Matlock, and J.G. Speer: *Mater. Sci. Eng. A*, 2006, vol. 438–440, pp. 25–34.
10. S. Samanta, P. Biswas, S. Giri, S.B. Singh, and S. Kundu: *Acta Mater*., 2016, vol. 105, pp. 390–403.
11. S. Samanta, P. Biswas, and S.B. Singh: *Scr. Mater*., 2017, vol. 136, pp. 132–35.
12. F. HajyAkbary, J. Sietsma, G. Miyamoto, T. Furuhara, and M.J. Santofimia: *Acta Mater*., 2016, vol. 104, pp. 72–83.
13. R. Abbaschian, L. Abbaschian, and R.E. Reed-Hill: in *Physical metallurgy principles*, 4 th., Cengage Learning, Stamford, USA, 2009, pp. 603–50.
14. H.K.D.H. Bhadeshia and R. Honeycombe: *Steels: Microstructure and Properties*, 4th ed. Butterworth-Heinemann, Oxford, 2017, pp. 217–36.
15. K. Iijima: *Trans. Jpn. Inst. Met*., 1963, vol. 4, pp. 52–56.
16. R.A. Grange: *Metall. Trans*., 1973, vol. 4, pp. 2231–44.
17. T. Heller and A. Nuss: *Ironmak. Steelmak*., 2005, vol. 32, pp. 303–08.
18. X. Gui, G. Gao, H. Guo, F. Zhao, Z. Tan, and B. Bai: *Mater. Sci. Eng. A*, 2017, vol. 684, pp. 598–605.
19. X.C. Xiong, B. Chen, M.X. Huang, J.F. Wang, and L. Wang: *Scr. Mater*., 2013, vol. 68, pp. 321–24.
20. W.J. Dan, W.G. Zhang, S.H. Li, and Z.Q. Lin: *Comput. Mater. Sci*., 2007, vol. 40, pp. 101–07.
21. V.F. Zackay, E.R. Parker, and D. Fahr: *ASM Trans*., 1967, vol. 60, pp. 252–59.
22. D.K. Matlock and J.G. Speer: in *Microstructure and texture in steels and other materials*, A. Halder, S. Suwas, and D. Bhattacharjee, eds., Springer, London, 2009, pp. 185–205.
23. Z.J. Xie, Y.Q. Ren, W.H. Zhou, J.R. Yang, C.J. Shang, and R.D.K. Misra: *Mater. Sci. Eng. A*, 2014, vol. 603, pp. 69–75.
24. E. De Moor, J.G. Speer, D.K. Matlock, J.-H. Kwak, and S.-B. Lee: *ISIJ Int*., 2011, vol. 51, pp. 137–44.
25. S. Samanta, S. Das, D. Chakrabarti, I. Samajdar, S.B. Singh, and A. Haldar: *Metall. Mater. Trans. A*, 2013, vol. 44A, pp. 5653–64.
26. S. Kumar: *Mater. Sci. Technol*., 2022, vol. 38, pp. 663–75.
27. Y. Toji, G. Miyamoto, and D. Raabe: *Acta Mater*., 2015, vol. 86, pp. 137–47.
28. S.M.C. Van Bohemen and J. Sietsma: *Mater. Sci. Technol*., 2009, vol. 25, pp. 1009–12.
29. P. Maynier, J.D. Manager, and P. Bastien: in *Hardenability Concepts with Applications to Steel*, D.V. Doane and J.S. Kirkaldy, eds., TMS-AIME, Warrendale, PA, 1977, pp. 163–78.
30. K.W. Andrews: *J. Iron Steel Inst*., 1965, vol. 203, pp. 721–27.
31. D.P. Koistinen and R.E. Marburger: *Acta Metall*., 1959, vol. 7, pp. 59–60.
32. K. Sugimoto, M. Kobayashi, and S. Hashimoto: *Metall. Trans. A*, 1992, vol. 23A, pp. 3085–91.
33. M.Y. Sherif, C.G. Mateo, T. Sourmail, and H.K.D.H. Bhadeshia: *Mater. Sci. Technol*., 2004, vol. 20, pp. 319–22.
34. S. Kumar and S.B. Singh: *Materialia*, 2021, vol. 18, 101135.
35. S. Kumar and S.B. Singh: *Mater. Charact*., 2023, vol. 196, 112561.
36. D.T. Pierce, D.R. Coughlin, K.D. Clarke, E. De Moor, J. Poplawsky, D.L. Williamson, B. Mazumder, J.G. Speer, A. Hood, and A.J. Clarke: *Acta Mater*., 2018, vol. 151, pp. 454–69.
37. E.J. Seo, L. Cho, and B.C. De Cooman: *Metall. Mater. Trans. A*, 2015, vol. 46A, pp. 27–31.
38. H.K.D.H. Bhadeshia and D.V. Edmonds: *Met. Sci*., 1983, vol. 17, pp. 411–19.
39. E. De Moor, J.G. Speer, D.K. Matlock, C. Föjer, and J. Penning: *Proc. Mater. Sci. Technol*., 2009, pp. 1554–63.

40. J. Kähkönen, D.T. Pierce, J.G. Speer, E. De Moor, G.A. Thomas, D. Coughlin, K. Clarke, and A. Clarke: *J. Mater.*, 2016, vol. 68, pp. 210–15.
41. T. Gladman: *The Physical Metallurgy of Microalloyed Steels*, Institute of Materials, London, 1997.
42. A.M. Streicher, J.G. Speer, D.K. Matlock, and B.C. De Cooman: in *Proceedings of the International Conference on Advanced High-Strength Sheet Steels for Automotive Applications*, J.G. Speer, ed., AIST, Warrendale, PA, 2004, pp. 51–62.
43. G.A. Thomas, E. De Moor, and J.G. Speer: in *Proceedings of the international symposium on new developments in advanced high--strength sheet steels*, E. De Moor, H.J. Jun, J.G. Speer, and M. Merwin, eds., AIST, Warrendale, PA, 2013, pp. 153–65.
44. D.T. Pierce, D.R. Coughlin, D.L. Williamson, K.D. Clarke, A.J. Clarke, J.G. Speer, and E. De Moor: *Acta Mater.*, 2015, vol. 90, pp. 417–30.
45. M.F. Gallagher, J.G. Speer, D.K. Matlock, and N.M. Fonstien: in *Proceedings of the 44th Mechanical Working and Steel Processing Conference*, Iron and Steel Society, Warrendale, PA, 2002, pp. 153–72.
46. J. Mahieu, S. Claessens, and B.C. De Cooman: *Metall. Mater. Trans. A*, 2001, vol. 32A, pp. 2905–08.
47. A. Grajcar, R. Kuziak, and W. Zalecki: *Arch. Civil Mech. Eng.*, 2012, vol. 12, pp. 334–41.
48. K. Kim and S.J. Lee: *Mater. Sci. Eng. A*, 2017, vol. 698, pp. 183–90.
49. E.J. Seo, L. Cho, and B.C. De Cooman: *Metall. Mater. Trans. A*, 2014, vol. 45A, pp. 4022–37.
50. A.M. Llopis: University of California, Berkeley, 1977.
51. V.S. Dwivedi, B.K. Jha, R. Avtar, and G. Thomas: *Key Eng. Mater.*, 1993, vol. 84–85, pp. 406–36.
52. J.G. Speer, D.K. Matlock, A.M. Streicher, F. Rizzo, and G. Krauss: in *Austenite formation and decomposition*, E.B. Damm and M.J. Merwin, eds., TMS/ISS, Warrendale, PA, 2003, pp. 505–22.
53. S.M.C. Van Bohemen: *Mater. Sci. Technol.*, 2012, vol. 28, pp. 487–95.
54. F. Gerdemann: *Microstructure and Hardness of 9260 Steel Heat Treated by the Quenching and Partitioning Process, Aachen University of Technology (RWTH), Dipl. Thesis*, 2004.
55. E.J. Seo, L. Cho, and B.C. DeCooman: *Metall. Mater. Trans. A*, 2016, vol. 47A, pp. 3797–3802.
56. A.J. Clarke, J.G. Speer, M.K. Miller, R.E. Hackenberg, D.V. Edmonds, D.K. Matlock, F.C. Rizzo, K.D. Clarke, and E. De Moor: *Acta Mater.*, 2008, vol. 56, pp. 16–22.
57. L. Cho, E.J. Seo, and B.C. De Cooman: *Scr. Mater.*, 2016, vol. 123, pp. 69–72.
58. M. Hillert and J. Ågren: *Scr. Mater.*, 2005, vol. 52, pp. 87–88.
59. J. Wang and S. Van der Zwaag: *Metall. Mater. Trans. A*, 2001, vol. 32A, pp. 1527–39.
60. O. Kriesement and F. Wever: in *Mechanism of Phase Transformations in Metals, Monograph and Rep. Ser. No. 18*, Institute of Metals, London, U.K., 1956, pp. 253–63.
61. H.K.D.H. Bhadeshia: *Bainite in Steels: Theory and Practice*, 3rd ed. Maney Publishing, Leeds, 2015.
62. J.G. Speer, F.C. Rizzo Assunção, D.K. Matlock, and D.V. Edmonds: *Mater. Res.*, 2005, vol. 8, pp. 417–23.
63. Y. Toji, H. Matsuda, M. Herbig, P.P. Choi, and D. Raabe: *Acta Mater.*, 2014, vol. 65, pp. 215–28.
64. S.M. Hasan: Indian Institute of Technology Kharagpur, India, 2019.
65. H.K.D.H. Bhadeshia: *Acta Metall.*, 1980, vol. 28, pp. 1103–14.
66. S.J. Matas and R.F. Hehemann: *TMS-AIME*, 1961, vol. 221, pp. 179–85.
67. E. De Moor and J.G. Speer: in *Automotive steels Design, Metallurgy, Processing and Applications*, R. Rana and S.B. Singh, eds., 2017, pp. 289–316.
68. W. Steven and A.G. Haynes: *J. Iron Steel Inst.*, 1956, vol. 183, pp. 349–59.
69. M. Peet and H.K.D.H. Bhadeshia: *MUCG83, Phase Transform. complex Prop. group, Dep. Mater. Sci. Metall. Univ. Cambridge, Cambridge, U.K.*.
70. C. García de Andrés, F.G. Caballero, and C. Capdevila: *Mater. Charact.*, 2003, vol. 49, pp. 121–27.
71. D. Chakrabarti, C. Davis, and M. Strangwood: *Mater. Charact.*, 2007, vol. 58, pp. 423–38.
72. R.A. Young: *Oxford Univ. Press. London*, 2002, pp. 1–111.
73. D.J. Dyson and B. Holmes: *J. Iron Steel Inst.*, 1970, vol. 208, pp. 467–74.
74. H.K.D.H. Bhadeshia, S.A. David, J.M. Vitek, and R.W. Reed: *Mater. Sci. Technol.*, 1991, vol. 7, pp. 686–98.
75. I. Stark, G.D.W. Smith, and H.K.D.H. Bhadeshia: *Metall. Trans. A*, 1990, vol. 21A, pp. 837–44.
76. E.V. Pereloma, I.B. Timokhina, M.K. Miller, and P.D. Hodgson: *Acta Mater.*, 2007, vol. 55, pp. 2587–98.
77. K. Venkateswarlu, M. Sandhyarani, T.A. Nellaippan, and N. Rameshbabu: *Procedia Mater. Sci.*, 2014, vol. 5, pp. 212–21.
78. G.K. Williamson and R.E. Smallman: *Philos. Mag.*, 1956, vol. 1, pp. 34–46.
79. L. Cheng, C.M. Brakman, B.M. Korevaar, and E.J. Mittemeijer: *Metall. Trans. A*, 1988, vol. 19A, pp. 2415–26.
80. S. Kumar, S. Samanta, and S.B. Singh: *Mater. Charact.*, 2022, vol. 191, 112049.
81. H.I. Aaronson, W.T. Reynolds, G.J. Shiflet, and G. Spanos: *Metall. Trans. A*, 1990, vol. 21A, pp. 1343–80.
82. G. Krauss: *Mater. Sci. Eng. A*, 1999, vol. 273–275, pp. 40–57.
83. A.J. Clarke, M.K. Miller, R.D. Field, D.R. Coughlin, P.J. Gibbs, K.D. Clarke, D.J. Alexander, K.A. Powers, P.A. Papin, and G. Krauss: *Acta Mater.*, 2014, vol. 77, pp. 17–27.
84. G. Krauss: D.V. Doane and J.S. Kirkaldy, eds., AIME, Warrendale, PA, 1978, pp. 229–48.
85. J. Hidalgo and M.J. Santofimia: *Metall. Mater. Trans. A*, 2016, vol. 47A, pp. 5288–5301.
86. S.M.C. Van Bohemen and J. Sietsma: *Mater. Sci. Technol.*, 2014, vol. 30, pp. 1024–33.
87. S.J. Lee and K.S. Park: *Metall. Mater. Trans. A*, 2013, vol. 44A, pp. 3423–27.
88. H.S. Yang and H.K.D.H. Bhadeshia: *Scr. Mater.*, 2009, vol. 60, pp. 493–95.
89. E. Jimenez-Melero, N.H. van Dijk, L. Zhao, J. Sietsma, S.E. Offerman, J.P. Wright, and S. van der Zwaag: *Scr. Mater.*, 2007, vol. 56, pp. 421–24.
90. S.J. Lee and C.J. Van Tyne: *Metall. Mater. Trans. A*, 2012, vol. 43A, pp. 422–27.
91. R. Ranjan and S.B. Singh: *Metall. Mater. Trans. A*, 2018, vol. 49A, pp. 4474–83.
92. A. Navarro-López, J. Sietsma, and M.J. Santofimia: *Metall. Mater. Trans. A*, 2016, vol. 47A, pp. 1028–39.
93. Y. Toji, H. Matsuda, and D. Raabe: *Acta Mater.*, 2016, vol. 116, pp. 250–62.
94. S.M. Hasan, S. Kumar, D. Chakrabarti, and S.B. Singh: *Philos. Magn.*, 2020, vol. 100, pp. 797–821.
95. M.J. Santofimia, T. Nguyen-Minh, L. Zhao, R. Petrov, I. Sabirov, and J. Sietsma: *Mater. Sci. Eng. A*, 2010, vol. 527, pp. 6429–39.
96. H.K.D.H. Bhadeshia and D.V. Edmonds: *Acta Metall.*, 1980, vol. 28, pp. 1265–73.
97. S.M.C. Van Bohemen and D.N. Hanlon: *Int. J. Mater. Res.*, 2012, vol. 103, pp. 987–91.
98. B.D. Cullity: *Elements of X-ray Diffraction*, Addison-Wesley Publishing Co Inc, Massachusetts, 1978.
99. S.B. Singh and H.K.D.H. Bhadeshia: *Mater. Sci. Eng. A*, 1998, vol. 245, pp. 72–79.
100. G.A. Thomas, F. Danoix, J.G. Speer, S.W. Thompson, and F. Cuvilly: *ISIJ Int.*, 2014, vol. 54, pp. 2900–06.
101. H.Y. Li, X.W. Lu, W.J. Li, and X.J. Jin: *Metall. Mater. Trans. A*, 2010, vol. 41A, pp. 1284–1300.
102. S. Hashimoto, S. Ikeda, K. Sugimoto, and S. Miyake: *ISIJ Int.*, 2004, vol. 44, pp. 1590–98.
103. S. Kang, J.G. Speer, D. Krizan, D.K. Matlock, and E. De Moor: *Mater. Des.*, 2016, vol. 97, pp. 138–46.
104. E. Jimenez-Melero, N.H. van Dijk, L. Zhao, J. Sietsma, S.E. Offerman, J.P. Wright, and S. van der Zwaag: *Acta Mater.*, 2007, vol. 55, pp. 6713–23.
105. G. Gao, H. Zhang, X. Gui, P. Luo, Z. Tan, and B. Bai: *Acta Mater.*, 2014, vol. 76, pp. 425–33.
106. P.J. Jacques, J. Ladrière, and F. Delannay: *Metall. Mater. Trans. A*, 2001, vol. 32A, pp. 2759–68.

107. O. Muránsky, P. Šittner, J. Zrník, and E.C. Oliver: *Acta Mater.*, 2008, vol. 56, pp. 3367–79.
108. B. Fu, W.Y. Yang, Y.D. Wang, L.F. Li, Z.Q. Sun, and Y. Ren: *Acta Mater.*, 2014, vol. 76, pp. 342–54.
109. F.B. Pickering: *Physical Metallurgy and Design of Steels*, Applied Science Publishers, Essex, 1978.
110. S.B. Singh, H.K.D.H. Bhadeshia, D.J.C. Mackay, H. Carey, and I. Martin: *Ironmak. Steelmak.*, 1998, vol. 25, pp. 355–65.
111. E.J. Seo, L. Cho, Y. Estrin, and B.C. De Cooman: *Acta Mater.*, 2016, vol. 113, pp. 124–39.